DELFT UNIVERSITY OF TECHNOLOGY

MATERIALS SCIENCE AND ENGINEERING

MASTER THESIS

DFT calculation of NMR parameters for the K doped $CsPbF_3$ solid-state ionic conductor

A small step toward a green vigor

Yixuan Zhang
Student number: 5556600

Supervisors:
Pedro Braga Groszewicz - SEE
Jouke Heringa - TNW
Alexandros Vasileiadis - SEE
Marcel Sluiter - MSE

August 24, 2023

Abstract

The lack of a decent solid-state ionic conductor has hindered the large-scale application of solid-state batteries, which are considered to be the potential game changer for energy transition. The recently reported K doping $CsPbF_3$ material system has shed light on this problem. This material possesses high ionic conductivity and a wide electrochemical stability window at the same time, making it a highly promising candidate for the next-generation fluoride ion solid-state battery. In order to have a clearer understanding of the structural information of this material and to find out what contributes to the outstanding properties it demonstrates, this thesis project uses Density functional theory(DFT) to calculate its ground state properties. Meanwhile, to better understand its local structure, the Nuclear magnetic resonance(NMR) parameters for this material are also calculated using DFT and analyzed in detail. Results generated from the calculations suggest that the coulombic interaction can be utilized to explain the structural deformation upon doping K into the $CsPbF_3$ system. Additionally, the analysis of the optimized cell structure indicates a tendency for the material system to go through a cubic to tetragonal phase transition, which reproduces the trend observed experimentally and offers a potential explanation for the driving force behind it. Further investigation using Nudged elastic band calculations(NEB) also reveals a relatively low energy barrier for vacancies to diffuse in the crystal structure, which provides insight into the high ionic conductivity of this material. The findings manifested in this thesis project could potentially offer improvement directions for the K-doped $CsPbF_3$ system and contribute to the development of other solid-state ionic conductors.

Contents

1 Introduction

August 1st, 2023, Xingtai, a city about 400 kilometers south of Beijing, has just experienced 1003.0 mm of rainfall in two days, which equals the normal amount of rainfall for that city in two years.(China Meteorological Administration, 2023) Beijing also experienced the heaviest rainfall in 140 years at the same time.(Reuters, 2023) Additionally, it has just been officially confirmed that the past July is the hottest month ever documented.(World Meteorological Organization, 2023) When writing this thesis, the ongoing record-breaking wildfire season in Canada has already burned approximately 13.5 million hectares of land, more than the size of three Netherlands combined.(NASA Earth Observatory, 2023) These are just some examples that have happened very recently. If we recall, extreme weather patterns like these are becoming more and more "normal" under the condition of climate change, the records are being broken constantly. We can witness this happening every year and it is getting even worse and worse. What should we do?

Throughout human history, people have been constantly searching for enough energy to power societies. With the explosive technology development in the past few centuries, a tremendous amount of energy is required. However, the mass exploitation of traditional fossil fuel-based energy is considered the main reason behind climate change. Floods, wildfires, drought, heatwaves, and other extreme weather are not rare anymore, which leads to severe consequences and significantly influences the survival of human beings. To tackle this, something needs to be changed fast in the current energy system.

But how do we balance the pursuit of more energy and the importance of protecting the climate and eventually protecting ourselves? The answer would be to go through an energy transition. To replace fossil fuel-based energy with renewables such as solar and wind energy. This could deeply shift how we view energy and how we acquire energy as well as potentially paving the stepping stone for the next technological breakthrough. By achieving this ambitious energy transition target, we can truly obtain a sufficient amount of clean energy without sacrificing the environment, and eventually realize a more sustainable way to live and develop.

Despite all the benefits brought by renewable energy, it is usually intermittent and unstable. For example, solar energy is mainly produced during the day and during summer. Considering that the consumption pattern is usually predictable and the big demand at night and during winter, a solar energy dominated energy system can bring some extra trouble, especially when compared with the current fossil fuel based energy system. To deal with this dilemma, suitable energy storage methods are essential to serve as a buffer and important backup. By incorporating energy storage with renewable energy generations, it can balance production and consumption thus making the large-scale employment of renewable energy to be feasible. It is without doubt that energy storage is a vital ingredient for energy transition.

Batteries, compressed air energy storage, pumped hydro energy storage, and energy stored in chemical agents such as hydrogen or ammonia are all promising methods for the storage of energy in the short term or long term.(Koohi-Fayegh & Rosen, 2020) Depending on the specific field of application, certain methods could be preferred over others. But generally speaking, among all the various types of energy storage methods, batteries stand out due to their technology readiness as well as the broad range of application circumstances. Electric vehicles are now becoming one of the symbols for the energy transition, of which batteries are the key. More and more stationary energy storage solutions operated by batteries are being built in households or near the renewable energy generation sites. Extensive research has been carried out non-stop to search for a type of battery with a better and better performance.

The solid-state battery is considered one of the most promising battery types. It can play an important role in the future energy storage market upon mass applications and possesses several unique advantages.(Janek & Zeier, 2016)(Pasta et al., 2020) As the name suggests, the solid-state battery consists of a solid-state electrolyte instead of a liquid electrolyte. This could provide solid-state batteries with higher energy density, smaller size, and enhanced safety properties compared to the current Li-ion batteries that are dominating the market. To put it more specifically, solid-state batteries do not pose risks such as flammability, explosion, or volatility. Even if the separator of the solid electrolyte is punctured, it will not spontaneously ignite like what would happen to the liquid-based battery. These advantages have drawn extensive attention worldwide and intensive research is being carried out at this moment. However, the development of solid-state batteries is still at an early stage due to various challenges in terms of the technology and manufacturing process.(Janek & Zeier, 2023) One of the major hurdles here is the lack of an efficient electrolyte material.(C. Li et al., 2021)

Solid-state electrolytes, also known as solid-state ionic conductors, play an important role in solid-state batteries, but the overall performance of current materials cannot meet the requirements of large-scale energy storage applications, despite some breakthroughs in individual indicators of solid-state lithium-ion conductors. (Dudney, West, & Nanda, 2015) Therefore, the search for a suitable solid-state ionic conductor with high ionic conductivity, good solid-solid interface contact properties, and low cost is of vital importance. To achieve this goal, a comprehensive understanding of the structure of the material and the ionic conducting mechanism would be the key.

1.1 Solid-state ionic conductors

Solid-state ionic conductors, which are applied as solid electrolytes, are materials that can conduct ions while remaining solid. These materials can be used in batteries, fuel cells, sensors, and other electrochemical devices. Good solid-state ionic conductors should have high ionic conductivity and enhanced safety performance enabling them to efficiently transport ions and therefore particularly suitable in the application of advanced electrochemical devices where stable and safe operation is required. Generally speaking, solid-state ionic conductors could also mitigate the risks associated with liquid electrolytes, such as leakage problems and dendrite formation, making devices more reliable and durable. Moreover, their properties can be tailored by tuning their composition and structure thus making them can be potentially applied to a wide range of applications.(Famprikis, Canepa, Dawson, Islam, & Masquelier, 2019)

However, solid-state ionic conductors are still in their early phase of research and there is still some distance from mass applications. Several challenges need to be further tackled, including but not limited to the discovery of cost-effective synthetic methods and materials with enhanced interfacial stability and performance. Ongoing research and development efforts are aimed at these challenges and dedicated to building a better understanding of the fundamental structure and property correlations .(Famprikis et al., 2019)

Solid-state ionic conductors can be divided into various types, including fluorides, oxides, sulfides, etc., and can be composed of elements such as lithium, sodium, potassium, and cesium. These different materials also have different crystal structures, such as perovskite, garnet, fluorite, or NASICON structure. In general, those materials that exhibit high ionic conductivity are very useful and suitable as solid electrolytes in all-solid-state batteries and fuel cells. It is important to understand why materials exhibit high ionic conductivity with some specific structures or chemical compositions.(Morgan, 2021) By understanding the factors that promote fast-ionic conduction in certain solid electrolytes, people can formulate general design principles to create new materials with improved ionic conductivity and lower cost. However, developing a detailed quantitative description of the ion transport behavior in ionic conductors can be challenging due to the complicated ion transport mechanisms. That is also part of the reason why ionic conducting materials have drawn much attention since the 19th century, but the underlying atomic-scale physics behind this behavior remains an incompletely resolved scientific question. (Tuller & Moon, 1988)

Various previous studies have looked into many factors affecting ionic conduction in solid electrolytes aiming at a comprehensive understanding of its conduction mechanisms. For example, part of the main focus of this topic is to find out what role the crystallographic barriers in the crystal structure play in terms of conducting ions.(Kraft et al., 2017) Studies also paid a lot of attention to the concept of frustration, where the energy considerations prevent the mobile ions from adopting a single-ordered low-energy configuration.(Morgan, 2021)(Wood et al., 2021) It is also found that some materials exhibit fast ion conduction due to specific host framework dynamics, such as kinetic bottlenecks coupled with charged ion motion or polyanion rotation.(Goodenough, 1984) Research also suggested that the vibrational properties of fast ionic conductors could also play an important role in determining the ionic conducting behavior, which can also influence the correlation between a simple descriptor calculated from the vibrational dynamic density and the ionic conductivity determined from materials with similar structures.(Kamitsos, Karakassides, & Chryssikos, 1986) Moreover, phonons in solid electrolytes change dramatically when transitioning from a low-temperature poorly conducting phase to a high-temperature "superionic" phase, which suggests that phonons could also be very relevant and important for understanding the mechanism behind.(Morgan, 2021)(Muy, Schlem, Shao-Horn, & Zeier, 2021)

In a nutshell, for a broad class of materials, ranging from Li^+ conductors in the solid-state lithium-ion battery to O^{2-} conductors in solid oxide cells, up to metal fluorides for F^- conduction in the alternative, anion-based solid-state batteries, the understanding of the structure of the solid-state ionic conductors and their exact mechanism of ionic conduction particularly is still under investigation. It can be foreseen that this will remain to be the frontier of research toward clean energy applications. Many informative research techniques and methods will be exploited for this topic.

To better understand the materials' micro- or macrostructure, suitable materials characterization methods are essential. Techniques like X-ray diffraction (XRD) are often used to obtain that kind of information. Despite that they are particularly useful for certain material systems, for instance, crystals, they could also be restricted for investigating certain cases, such as the research involving glass materials or the study of materials with partial disorder due to aliovalent doping which is a commonly used strategy for modifying ionic conductors. Under these circumstances, other techniques like Nuclear Magnetic Resonance spectroscopy (NMR) could play an important role.

Generally speaking, NMR has the advantage of being a non-destructive method that preserves the integrity of the sample, whereas XRD often requires the sample to be prepared in a specific way. Additionally, NMR is highly sensitive to specific elements such as hydrogen, carbon, lithium, and fluorine. It can also provide detailed insight into the atomic and molecular structure of materials. Moreover, the wide range of sub-techniques NMR covers, including solid-state NMR, can be tailored to different material types and systems. Hence, NMR could be a well-suited method for studying solid-state ionic conductors.

Among the various types of technologies of NMR, the solid-state NMR spectroscopy technique can be particularly helpful in terms of providing details of the atomic-level environment of materials. However, high-resolution spectra are often difficult to obtain and difficulties are also presented when interpreting and assigning the spectra. In this case, DFT calculations can be used to assist the understanding of NMR spectroscopy when studying the properties of disordered materials. DFT calculation of NMR parameters is a highly effective method to study the local structure, disorder, and dynamics of solids, as well as to provide insight into the atomic-scale environment. The use of this method can facilitate a more complete understanding of the structure of materials. (Ashbrook & Dawson, 2013) Intensive research has been carried out in the field of DFT calculation of NMR parameters for many types of materials and their specific applications. The next sections will briefly introduce two representative studies where the researchers used the method of DFT calculation of NMR parameters to study the structure and properties of the solid-state ionic conductors, namely Li^+ and O^{2-} conductors.

1.1.1 Li^+ solid-state ionic conductors

In this study, Szczuka et al. (Szczuka et al., 2022) studied an $xLi_3P-(1-x)Li_2S$ metastable solid solution material, which can be potentially used as a stable and highly conductive solid electrolyte for Li-ion solid-state batteries. The researchers successfully investigated the material's structure and conduction mechanism using the DFT calculation of NMR parameters method.

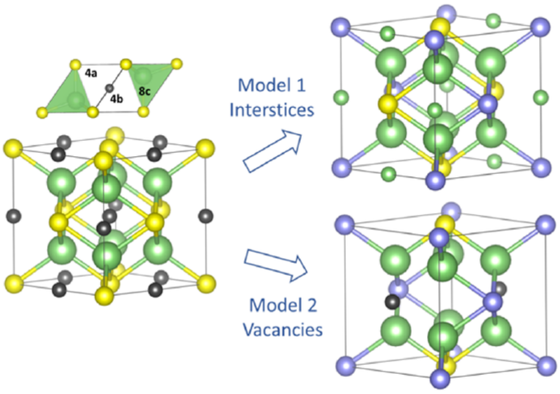

Figure 1: Two possible structural models for the Li_2S-Li_3P solid solutions. Retrieved from (Szczuka et al., 2022)

They first carried out the XRD measurement and proposed two structure models that are both consistent with the XRD pattern (Fig 1), where Model 1 has occupied octahedral voids by additional Li ions while Model 2 doesn't. Then they performed NMR measurements which can be seen in Fig 2. The ^7Li spectra showed that the Li-S-P system is a continuous solid solution of Li_2S type because the exact shift is determined by the Li_2S to Li_3P ratio. Also due to the appearance of a significant amount of excess Li_2S at x = 0.33, the researchers concluded that the kinetic limit of the solid solution range is x > 0.33. From the ^{31}P NMR results, the researchers observed a correlation between the ratio of the starting binaries and the linewidth, the peak gets broader as the phosphorus content goes up, which is being ascribed to a more diverse phosphorus environment like the appearance of additional Li ions and possible second shell effects, which can also be backed up by the line shape changing from Lorentzian to Gaussian.

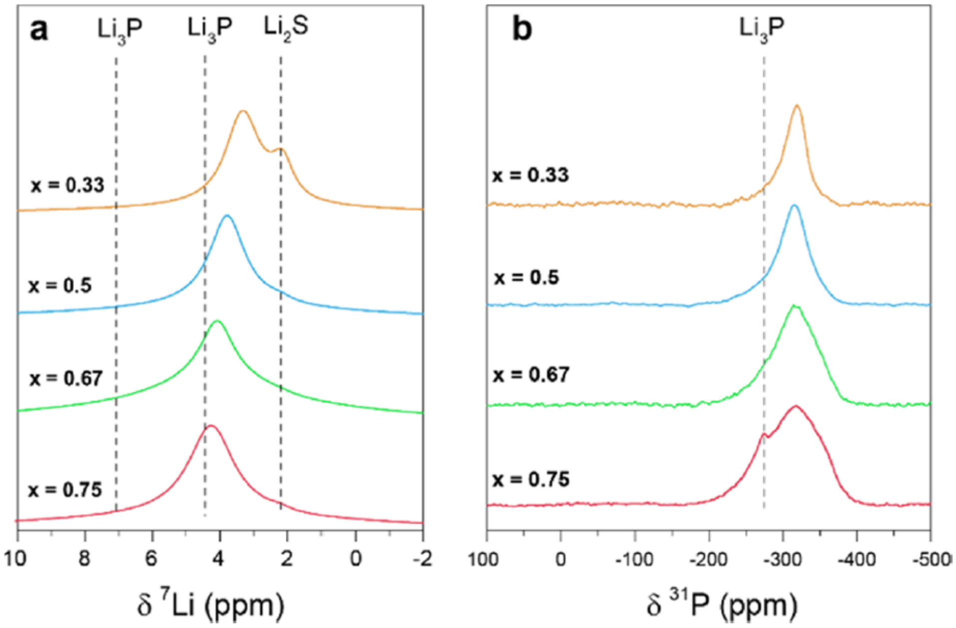

Figure 2: Room temperature (a) ^7Li and (b) ^{31}P MAS NMR spectra, at a 50 kHz spinning speed, of the solid solutions in the system $xLi_3P-(1-x)Li_2S$. Retrieved from (Szczuka et al., 2022)

Since the NMR measurements here still cannot tell exactly which model is a better description of the material's structure in reality. The researchers further used DFT to calculate the NMR parameters of this material and compared the calculated spectrum with the experimental one. The calculation results showed that Model 1 fits better with the experimental results as can be seen from Fig 3. Also considering that higher formation energy is required for phases generated by Model 2. This study concluded that in the composition range of 0.39≤x≤0.75, this material is a solid solution of Li_2S anti-fluorite structure type, which has a fully occupied mixed S^{2-}/P^{3-} anion lattice. Since the voids of tetrahedrons and octahedrons are partially filled by Li ions, the vacancies left can enable Li-ion hopping. This makes this system exhibit high ionic conductivity and intrinsic redox stability for Li metal, as well as a facilitated Li-ion transport effect. In a nutshell, this study managed to propose insights into the material structure and conduction mechanism of a promising Li-ion solid-state ionic conductor using DFT to calculate its NMR parameters.

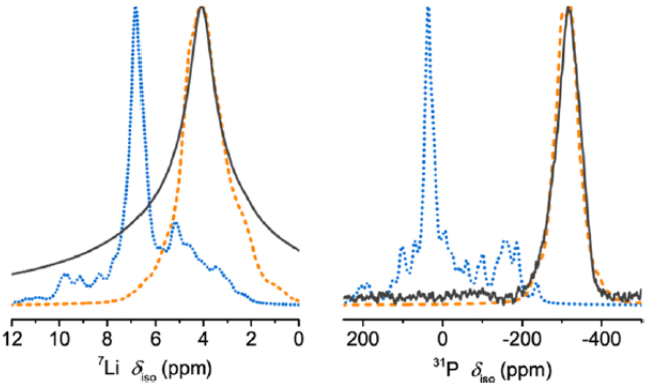

Figure 3: Predicted ^7Li and ^{31}P NMR spectra of the Li_8P_2S ternary, generated with the lowest energy DFT structures resulting from the two solid-solution models: Model 1 (orange, dashed) and Model 2 (blue, dotted), compared to the experimental spectra (black). Retrieved from (Szczuka et al., 2022)

1.1.2 O^{2-} solid-state ionic conductors

Another example is the study by Panchmatia et al,(Panchmatia et al., 2011) where they investigated the Si and Ge-based apatite compound $La_8Y_2Ge_6O_{27}$, a novel phosphorus compound with high oxide ion conductivity and oxygen excess, as a potential oxygen ion-conducting electrolyte for solid oxide fuel cells. The atomic-scale properties and conduction mechanisms of this material are still unclear previously. To shed light on these themes, the researchers investigated defect sites and conduction mechanisms in $La_8Y_2Ge_6O_{27}$ using the DFT calculation of NMR parameters method.

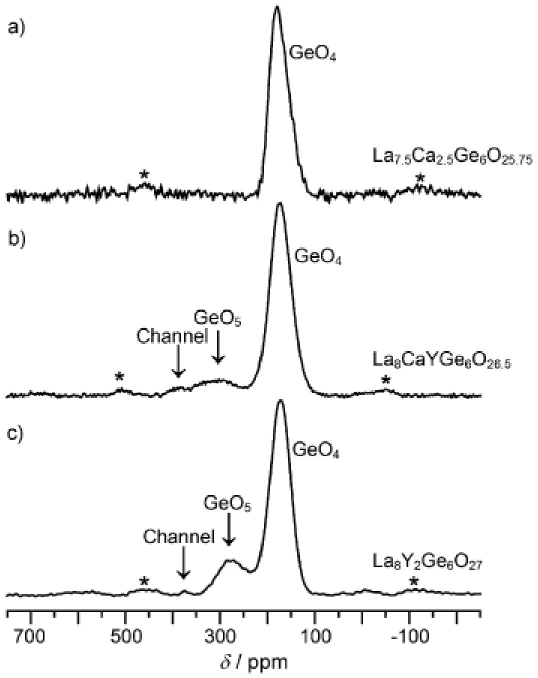

Figure 4: ^{17}O MAS NMR data at 54.22 MHz and assignments for a) $La_{7.5}Ca_{2.5}Ge_6O_{25.75}$, b)$La_8Y_2CaGe_6O_{26.5}$, and c)$La_8Y_2Ge_6O_{27}$. The asterisks denote the positions of spinning sidebands. Retrieved from (Panchmatia et al., 2011)

Apatite materials do not use vacancies as conductive defects like traditional fluorite and perovskite oxides, and the oxide ions at the interstitial sites are the main defects responsible for conduction, which makes it very challenging to understand the conduction mechanism. In this study, the researchers utilized ^{17}O MAS NMR to probe the local structure of oxide materials, revealing the increase of interstitial oxide ions. As shown in Fig 4, compared to (a), (b) and (c) consist of an additional downfield resonance peak, because the intensity goes up from (b) to (c) which links to an increase in oxygen relative composition, one can attribute this resonance to the presence of increasing interstitial oxide ions. However, how does the local structure look like exactly is still unclear. Therefore, DFT calculations were then used to analyze the positions of interstitial oxide ion sites in $La_8Y_2Ge_6O_{27}$, they used VASP for geometry optimization and GIPAW in CASTEP for calculating electric field gradient and isotropic shift. The results showed that the binding of interstitial oxide ions preferentially occurs between two GeO_4 tetrahedra, leading to the local relaxation of the tetrahedrons. As can be seen from Fig 5, the calculations are sensitive enough to predict the small shift separation between the GeO_5 units and the framework GeO_4 tetrahedra, which indicates the appearance of the GeO_5 units are the reason behind the additional downfield resonance in the NMR spectra. The results of this study showed that interstitial oxide ion defects are closely related to the germanium in the compound, specifically the formation of pentacoordinate germanium. Furthermore, this study also revealed that oxygen ion transport occurs through a cooperative mechanism involving framework tetrahedra, which includes a novel substitution-mediated conduction mechanism that facilitates oxygen ion transport despite the absence of open conduction pathways.

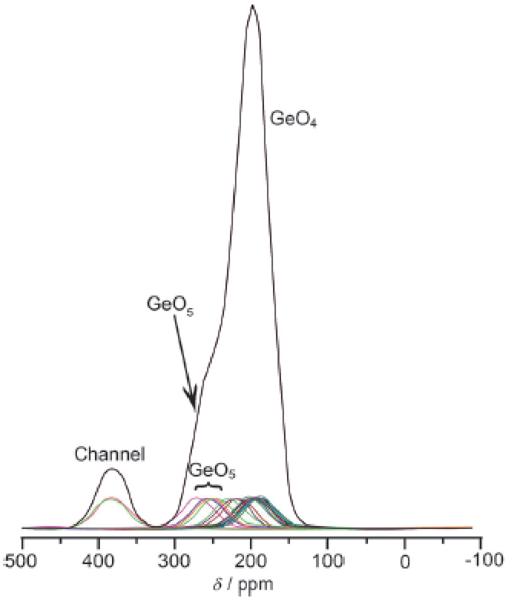

Figure 5: Simulated ^{17}O NMR spectrum for $La_8Y_2Ge_6O_{27}$ from DFT calculations. The scaling of the ^{17}O chemical shifts was undertaken at both the low-field (channel oxygen) and high-field (framework GeO_4) ends to facilitate comparison with the measured data (Fig 4). The calculations predict the small shift separation between the GeO_5 units (interstitial induced) and framework GeO_4 tetrahedra. Retrieved from (Panchmatia et al., 2011)

In conclusion, this study contributes to a better understanding of defect sites and conduction mechanisms in apatite germanate. The researchers concluded that instead of some isolated interstitial oxide ions being loosely connected to GeO_4 tetrahedral, a GeO_5 unit is formed. This study reveals the atomic-scale environment and localizes interstitial oxide ion defects in apatite germanate. It may pave the way for the development of novel electrolytes with improved properties. These findings have important implications for the development of new oxide ion conductors for clean energy applications. Additionally, this study provides further evidence that computational methods such as molecular dynamics simulations and DFT calculations, combined with NMR, can provide valuable insights into the atomic-level properties of materials.

1.2 F^- solid-state ionic conductors and research questions

After a brief introduction of the Li^+ and O^{2-} solid-state ionic conductors, we shift the focus to another appealing candidate that is also important for the future solid-state batteries, the F^- solid-state ionic conductor. Since fluorine is the most electronegative element, thus fluorine ions are extremely stable. Also considering that it is not easy to form the corresponding simple substance, thus a safety hazard similar to dendrite growth in lithium batteries is less likely to happen for fluoride ion batteries. And generally speaking, the electrode material of fluoride-ion batteries can contribute several charges per chemical formula, so the theoretical energy density is very high. Additionally, the abundance of fluorine in the earth's crust is also relatively high, which is about 50 times more than that of lithium, the application prospects of fluoride ion batteries are very exciting. However, the actual performance of fluoride-ion batteries is still far from being comparable to that of lithium-ion batteries. This is mainly because the known fluoride-ion battery electrolytes either have very low ionic conductivity or a very small electrochemical stability window. This makes the constructed batteries not equipped with effective voltage to be used. A recently reported study has proposed a promising new material that can be employed as an effective solid-state fluoride ion conductor, which has again shed light on the potential application of fluoride ion batteries.

Wang et al. (Wang et al., 2022) synthesized a series of $CsPb_{1-x}K_xF_{3-x}$ materials by mechanical alloying method, where x = 0, 0.05, 0.10, 0.15, 0.20 (abbreviated as PK00, PK05, PK10, PK15, PK20, respectively). These materials all have an ABX_3 perovskite structure, in which the A site is occupied by Cs, the B site is occupied by Pb or K, and the X site is occupied by F. The study proposes that with the increase of the K content as an aliovalent doping element, the F sites that were originally occupied in $CsPbF_3$ begin to form vacancies, making ion transportation more efficient. But at the same time, the lattice constant also decreases with the increase of K content, thereby compressing the space available for ion migration in the lattice. The researchers proposed that if these two opposite effects can achieve an optimal balance in a certain composition, also considering the promotion of the anion migration by the $6s^2$ lone pair electrons in the outermost layer of Pb^{2+}, it is expected to achieve a higher ionic conductivity. This study indeed found that the conductivity reaches a maximum of 1.23 mS/cm^{-1} at room temperature at x = 0.10 (corresponding to PK10), which can be visualized in Fig. 6. This ionic conductivity is comparable to $PbSnF_4$ (0.5–1.6 mS/cm^{-1}), the fluoride ion conductors with the highest ionic conductivity currently. This number indicates that PK10 is able to support charge and discharge at room temperature. Meanwhile, the electronic conductivity of PK10 material is 1.6×10^{-7} S/cm^{-1}, which is much lower than its ionic conductivity. At the same time, theoretical calculations found that the PK10 solid electrolyte has a wide electrochemical stability window close to 2V, which was further verified by the linear sweep voltammetry test. Therefore, the solid electrolyte PK10 designed in this study has excellent comprehensive electrochemical performance, which is very promising to be used as a solid electrolyte in fluoride-ion batteries. Moreover, PK10 has also realized a stable and long-term cycle of all-solid-state fluoride-ion batteries at room temperature, and the battery capacity has experienced almost no attenuation after repeated charging and discharging for more than 4,500 hours.

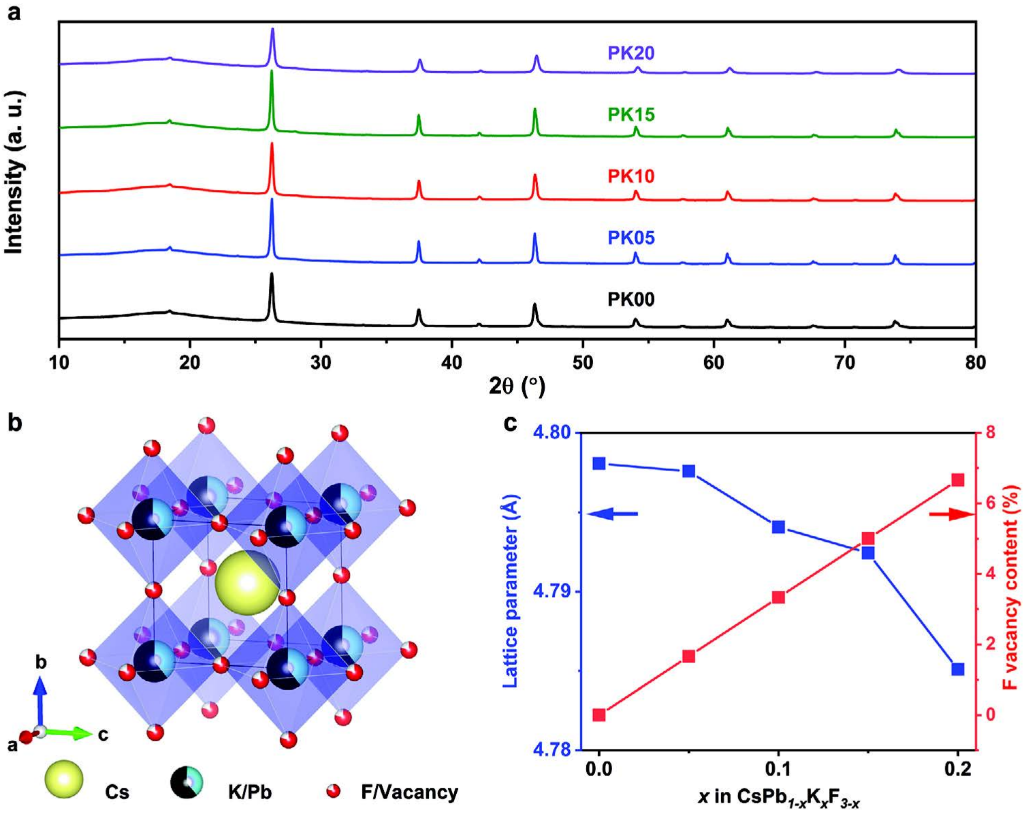

Figure 6: Crystal structures of $CsPb_{1-x}K_xF_{3-x}$. a) XRD patterns for PK00, PK05, PK10, PK15, and PK20. b) Unit cell of the $CsPb_{1-x}K_xF_{3-x}$ perovskite. c) Evolution of lattice parameters and F vacancy contents with composition. Retrieved from (Wang et al., 2022)

In short, the discovery of PK10 has overcome an important bottleneck for the fluoride ion battery, which makes this energy storage technology even more promising. But there is still something worth further investigating here, for example, What is the conduction mechanism and where are the conduction pathways for the hopping of fluoride ions? How to explain the achieved high ionic conductivity and can we use the findings here to assist us in searching for other material systems that are as good as or even more excellent than this one here?

A follow-up study by the same researchers also found out that upon doping K atoms into the $CsPbF_3$ structure to a certain composition, the material will undergo a phase transition from cubic to tetragonal, from the cubic structure of PK10 to the tetragonal structure of PK15, as can be seen from Fig 7. This could be the reason why the ionic conductivity goes down after K composition reaches 10%. But still, several questions also remain here, for instance, how do the atoms move along and what is the driving force behind this phase transition? Why the cubic structure could potentially be more favorable for ionic conduction than the tetragonal structure? Why does this phase transition happen at K composition in between 10-15% and what is the exact K composition for this change?

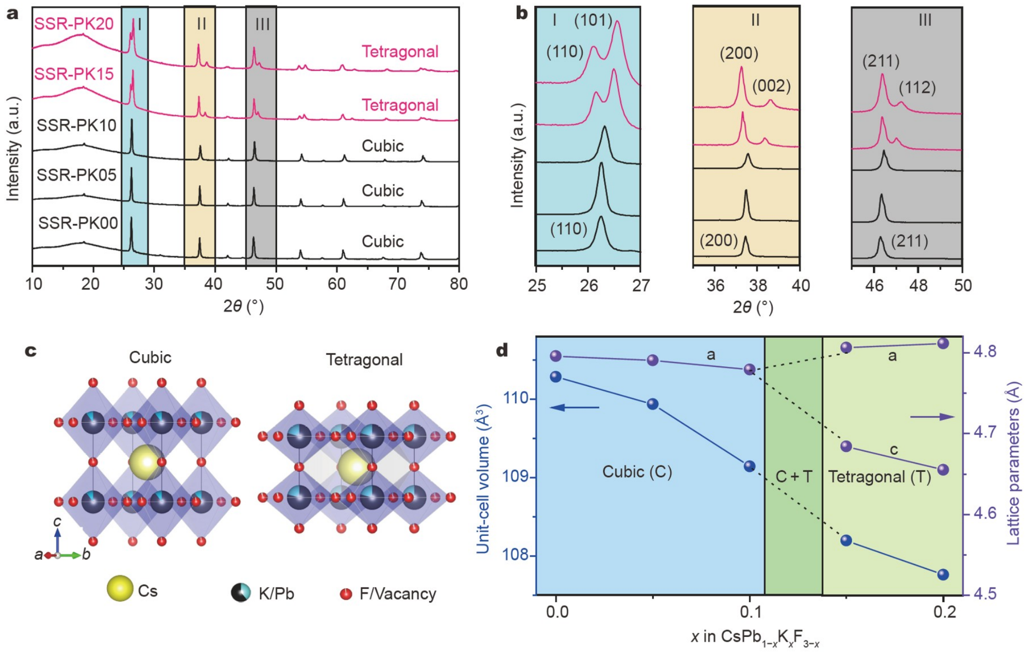

Figure 7: (a) XRD patterns of the $CsPb_{1-x}K_xF_{3-x}$ materials prepared by the solid-state reaction. (b) Enlarged view of regions I, II and III in (a). (c) Unit cells of the cubic (Pm3m) and tetragonal (P4/mmm) $CsPb_{1-x}K_xF_{3-x}$. The crystal structure was visualized using VESTA(Momma & Izumi, 2008). (d) Phase evolution and variation of unit-cell dimensions with composition for $CsPb_{1-x}K_xF_{3-x}$ materials prepared via the solid-state reaction. Retrieved from (Wang & Ma, 2022)

It is quite clear that multiple questions still remain for this material system despite that previous studies have already provided some insight into the structure and properties correlations of it as well as some important theoretical data.(Murtaza, Ahmad, Maqbool, Aliabad, & Afaq, 2011)(Boltalin, Rykov, & Korenev, 1990)(Boltalin, Korenev, & Sipachev, 2007)(Qian, Xu, & Tian, 2016) In order to better understand the local structure, as well as the reason for the good electrochemical performance, some NMR measurement has also been conducted already. However, the interpretation of the NMR spectrum is not straightforward. Under this circumstance, DFT could be very helpful, which will be the main method used in this master thesis to tackle the above-mentioned problems.

A literature review carried out previously as a preparation for this thesis work has shown that using DFT to calculate the NMR parameters of the materials of interest can be a very powerful and productive way in terms of understanding its structure and properties. This approach has been widely used for a big scope of materials and for a long time, the effectiveness has been deeply tested. Hence, in this thesis project, the same method is employed to study the previously mentioned questions about the K-doped $CsPbF_3$ material system with a focus on the following ones:

What would be the most favorable symmetries of the pure $CsPbF_3$ *material at different temperatures and what would be the driving force for the phase transitions it experiences?*

What structural information can be obtained for the K-doped $CsPbF_3$ *material from the DFT calculation of its NMR parameters?*

How to explain the high ionic conductivity measured experimentally for the K-doped $CsPbF_3$ *material?*

2 Research Methodology

This chapter will first briefly introduce some concepts regarding NMR and DFT. Then, the detailed research methods used for this thesis project will be presented, containing the necessary information needed to repeat the same calculation in order to obtain the exact same or close results. What will be mentioned here includes but is not limited to the input and parameters used for the individual research with respect to each subsection, how to obtain the data that are used for the calculations as well as how to process the data retrieved from the calculations etc.

2.1 Nuclear Magnetic Resonance spectroscopy

Nuclear Magnetic Resonance (NMR) is a commonly used non-destructive characterization technique with a wide range of applications. Compared with other common spectroscopic techniques, it provides atomic-level detailed information, such as the local structure and short-range order of materials, at a relatively higher resolution. NMR can detect substances both qualitatively and quantitatively, while also providing insight into their substance structure, and composition, and obtaining molecular dynamics information of substances and reactions. The principle of NMR is based on the interaction of the magnetic field applied by the instrument with the magnetic moment of the atomic nucleus. (Groszewicz, 2021) In NMR experiments, important information is obtained by analyzing data such as the peak position, peak shape, and peak intensity. NMR interaction parameters, such as chemical shift, dipole-dipole coupling constants, and quadrupole coupling constants, can be obtained from the measurement, which can be interpreted to provide information such as the bond lengths, bond angles, and spatial distribution of chemical bonds, which can contribute clear understanding of the material structure. (Bonhomme et al., 2012)

Within various types of techniques derived from NMR, solid-state NMR is an analytical method for studying solid-state samples. This method can be used to detect the interaction between the internal electromagnetic moment of the sample and the external electromagnetic field, so as to understand the relevant internal chemical environment of the sample and other information. It can also be used to detect the Zeeman interactions caused by external magnetic fields. This technique can be used to study the local structure of different solid materials, providing structural information at the atomic and molecular levels, and is therefore widely used in various fields such as batteries and catalysis. Solid-state NMR can provide detailed structural information on materials by analyzing the short- and medium-range interactions around different atomic nuclei. It can be used to analyze solid substances with high crystallinity, as well as the structure of solid or amorphous substances. It is a good complement to X-ray diffraction techniques in terms of materials research.(Duer, 2008)

In terms of the interpretation of the data retrieved from NMR measurements, changes in NMR spectra that detect molecular motions are due to the effects of these motions on the nuclear spin Hamiltonian. The NMR Hamiltonian is a mathematical representation of the interaction of energy levels and nuclear spins in a magnetic field and contains various parameters. For example, the chemical shift parameter is expressed in parts per million (ppm) relative to the frequency of a reference compound. It can reflect the local magnetic environment of an atomic nucleus depending on the specific electron density and molecular structure. It can also provide insights into the chemical composition and structural details of molecules. To put it simply, the chemical shift is a key parameter in NMR that provides qualitative information on the composition and type of species.

Another example is the quadrupole coupling constant, which characterizes the interaction between an atomic nucleus with a spin number greater than 1/2 and the electric field gradient in its local environment. This coupling results in the broadening of the NMR signal and provides relevant information about the symmetry and dynamics of the molecular system. The NMR Hamiltonian parameters are an important theoretical basis for applied NMR spectroscopy, which can be used to provide valuable information about molecular structures, dynamics, and their interactions. This then leads to the interpretation of these parameters to be one of the main tasks in NMR characterizations. (Hore, 2015)

2.1.1 Using DFT to calculate NMR parameters

DFT calculations can be utilized to predict NMR parameters such as the chemical shifts and coupling constants, especially for structurally complex materials. Considering the efficiency and cost-effectiveness of DFT, it can be used for a wide range of molecular systems including organic molecules, inorganic molecules, and biomolecules. It can also be used to study various NMR active nuclei such as hydrogen, carbon, and fluorine. To be specific, DFT calculations can provide detailed information about molecular structure and electronic properties that can help interpret NMR spectra thus enhancing the understanding of the materials structure. DFT can also be used to study the effect of some experimentally inaccessible conditions on NMR parameters, such as extremely high temperatures. Moreover, DFT has been proven by many studies that can be used to accurately predict NMR parameters, and the calculated results can be in good agreement with experimental data, which further proves its high value for NMR parameter prediction.

Using DFT to calculate NMR parameters is often performed in CASTEP (Segall et al., 2002), which mainly includes the following steps.(Clark et al., 2005) The first step is to input the initial information and to go through the structure geometry optimization for the materials of interest, by minimizing the total energy relative to the atomic position, the most stable state of the atoms in the material structure can be found, which could lead to more accurate NMR parameters calculated later. Next, an appropriate basis set needs to be chosen, which is very important for representing the electron wavefunctions of the atoms in the material. A suitable basis set should be able to accurately describe the electron density around the NMR active nucleus while taking into account the computational feasibility. The next step is to choose the appropriate DFT method and algorithm to calculate the various parameters of NMR. The choice of a specific method varies according to the material system under study. Common methods include Gauge-including atomic orbitals (GIAO), Linear Augmented Plane Wave (LAPW), Gauge Including Projector Augmented Waves (GIPAW), etc.(Charpentier, 2011) Then the calculated NMR parameters are compared with experimental data to assess their accuracy and reliability. This may involve comparing calculated chemical shifts and coupling constants to experimental NMR spectra or other measurements of the same molecule or similar materials. Finally, the obtained results can be used to interpret and analyze the structure and properties of the material of interest.

In summary, DFT can be very helpful in terms of helping to understand the NMR data obtained or to generate the experimentally inaccessible data directly. DFT calculation of NMR parameters is a powerful method being used to analyze the structure and properties of the materials. Under this circumstance, a thorough understanding of DFT is of vital importance, which will be the focus of the next chapter.

2.2 Density functional theory

First-principles computation is a computational method that is being widely used in materials science, physics, chemistry, and other fields. It takes advantage of the most fundamental laws and principles in physics to predict and simulate the ground state property of materials, molecules, and other systems. Typically, first-principles calculations involve the application of quantum mechanics to describe the behavior of atoms and electrons. Using mathematical algorithms, it can be used to predict things like the electronic structure, bond energy, thermodynamic properties, transport properties, and the total energy of the system of interest. Common first-principles methods include density functional theory, Hartree-Fock theory, etc. These methods are particularly useful for studying materials that are challenging or even impossible to study experimentally. They can be used to guide the design of new materials with specific properties and to facilitate the study of complex systems.(Maddox, 1988)

Density functional theory (DFT) is a widely used method of first-principles calculations. DFT uses only the electron density of a system to describe its ground state properties. To enable this happening, the Born-Oppenheimer approximation needs to be introduced first, it states that because of the big mass difference between nuclei and electrons, the motion of nuclei is negligible compared to the motion of electrons. Therefore, we can assume the nuclei to be fixed and only consider the electrons when solving the material's ground state properties. DFT exactly uses only the electron density to predict things such as the electronic band structure, chemical reactivity, and magnetism of materials by solving Schrödinger's equation below.

The time-independent, nonrelativistic Schrödinger equation is given by:

$$\hat{H}\psi(\mathbf{r}) = E\psi(\mathbf{r}) \tag{1}$$

Or:

$$-\frac{\hbar^2}{2m}\nabla^2\psi(\mathbf{r}) + V(\mathbf{r})\psi(\mathbf{r}) = E\psi(\mathbf{r}), \tag{2}$$

where:

$\hat{H}$ = Hamiltonian operator
$\psi(\mathbf{r})$ = Wavefunction
E = Energy of the system
$\mathbf{r}$ = Position vector
$\hbar$ = Reduced Planck's constant
m = Mass of the particle of interest
$V(\mathbf{r})$ = Electrostatic potential of the system
∇^2 = Laplacian operator

The exact definition of the Hamiltonian depends on the physical system described by Schrödinger's equation.(Sholl & Steckel, 2022) In some simple cases, such as particles in a box or harmonic oscillators, the Hamiltonian has a simple form, in which case Schrödinger's equation can be solved exactly. However, in cases involving multiple electrons interacting with multiple nuclei, the Schrödinger equation becomes more complex and may not be analytically solvable anymore.

For the situation where multiple electrons interact with multiple nuclei, Schrödinger's equation can be written by:

$$[-\frac{\hbar^2}{2m}\sum_{i=1}^{N}\nabla_i^2 + \sum_{i=1}^{N}V(\mathbf{r}_i) + \sum_{i=1}^{N}\sum_{j\neq i}U(\mathbf{r}_i,\mathbf{r}_j)]\psi(\mathbf{r}) = E\psi(\mathbf{r}) \tag{3}$$

Where:

$$\begin{aligned}
\psi(\mathbf{r}) &= \text{Wave function}\\
E &= \text{Energy of the system}\\
\hbar &= \text{Reduced Planck's constant}\\
m &= \text{Mass of the particle}\\
N &= \text{Number of particles in the system}\\
\nabla_i^2 &= \text{Laplacian operator on the } i\text{-th particle}\\
V(\mathbf{r}_i) &= \text{External potential acting on the } i\text{-th particle}\\
U(\mathbf{r}_i,\mathbf{r}_j) &= \text{Interaction potential between particles } i \text{ and } j
\end{aligned}$$

In this scenario where the exact solution cannot be found, DFT can be applied to solve Schrödinger's equation approximately. What justifies this are two key mathematical theorems established by Kohn and Hohenberg. The first theorem states that the ground state energy in Schrödinger's equation is uniquely determined by the electron density. This means that there is a one-to-one correspondence between the ground state wave function and the electron density. The second theorem defines an important property of functionals, which states that the electron density that minimizes the total energy is the true electron density corresponding to the full solution of the Schrödinger equation. Essentially, these two theorems show that the ground state energy E can be expressed as a functional of electron density, denoted E[n(r)], which is also why the method is called density functional theory. This finding suggests that electron density uniquely determines all properties at the ground state, including energy and wave function. This is a very important discovery that makes solving the Schrödinger equation a function of three spatial variables (the electron density) instead of 3N variables (the wave function), where N is the number of electrons.(Sholl & Steckel, 2022) When describing the electron density, different sets of functions are available, which are also referred to as the basis set. For periodic systems like an ionic conducting crystal, the plane wave basis set is often used, where the solution of Schrödinger's equation satisfies Bloch's theorem. Bloch's theorem states that for a particle in a periodic lattice potential, the wave function Ψ can be written as a product of a periodic function $u_k(r)$ and a plane wave $e^{ik\cdot r}$:

$$\Psi_k(r) = e^{ik\cdot r}u_k(r), \tag{4}$$

where k is the wave vector, r is the position vector, and $u_k(r)$ is a periodic function with the same periodicity as the lattice potential. $e^{ik \cdot r}$ in Bloch's theorem are also called plane waves, hence the calculations based on this theory are also called plane-wave calculations. Bloch's theorem is a fundamental concept in condensed matter physics that provides a powerful framework for understanding the behavior of wave functions in periodic structures.(Engel & Dreizler, 2011) It enables DFT to use the plane wave basis set to represent the electronic wave functions very accurately for periodic systems, which is exactly the focus of this thesis project.

Kohn and Sham further demonstrated that finding the correct electron density that represents the ground state of the system can be expressed in a way that involves solving a set of equations, each of which is related to an electron. This set of equations is called the Kohn-Sham equations.

The Kohn-Sham equations in density functional theory are given by:

$$[-\frac{\hbar^2}{2m}\nabla^2 + V_{\text{ext}}(\mathbf{r}) + V_{\text{H}}(\mathbf{r}) + V_{\text{XC}}(\mathbf{r})]\phi_i(\mathbf{r}) = \epsilon_i \phi_i(\mathbf{r}) \tag{5}$$

Where:

$$\begin{aligned}
V_{\text{ext}}(\mathbf{r}) &= \text{External potential} \\
V_{\text{H}}(\mathbf{r}) &= \text{Hartree potential} \\
V_{\text{XC}}(\mathbf{r}) &= \text{Exchange-correlation potential} \\
\phi_i(\mathbf{r}) &= \text{Kohn-Sham orbital} \\
\epsilon_i &= \text{Kohn-Sham orbital energy} \\
\mathbf{r} &= \text{Position vector} \\
\hbar &= \text{Reduced Planck's constant} \\
m &= \text{Mass of the particle} \\
\nabla^2 &= \text{Laplacian operator}
\end{aligned}$$

The Kohn-Sham equation involves three potentials, V_{ext}, V_H, and V_{XC}. The first potential represents the interaction between electrons and the collection of nuclei, while the second describes the Coulomb repulsion between the electron being considered and the total electron density determined by all electrons in the system. The third potential represents the contribution of exchange and correlation to the one-electron equation.(Sholl & Steckel, 2022) Therefore, in order to solve the Kohn–Sham equations, the exchange-correlation functional has to be specified, and many approximation methods exist here. For example, the local density approximation (LDA) uses only the local density at a given point to define the exchange-correlation functional, which is given by:

$$E_{\text{LDA}}[\rho] = \int \rho(\mathbf{r})\varepsilon_{\text{xc}}(\rho(\mathbf{r}))d\mathbf{r} \tag{6}$$

where:

$$\begin{aligned}
E_{\text{LDA}}[\rho] &= \text{LDA energy functional} \\
\rho(\mathbf{r}) &= \text{Electron density} \\
\varepsilon_{\text{xc}}(\rho(\mathbf{r})) &= \text{Exchange-correlation energy per electron as a functional of } \rho(\mathbf{r})
\end{aligned}$$

If taking the local electron density and the local gradient in the electron Density both into account, then another exchange-correlation functional can be established which is called the generalized gradient approximation (GGA).

The generalized gradient approximation (GGA) in density functional theory (DFT) is given by:

$$E_{\text{GGA}}[\rho] = \int \rho(\mathbf{r})\varepsilon_{\text{xc}}(\rho(\mathbf{r}), \nabla\rho(\mathbf{r}))d\mathbf{r} \tag{7}$$

where:

$$\begin{aligned} E_{\text{GGA}}[\rho] &= \text{GGA energy functional} \\ \rho(\mathbf{r}) &= \text{Electron density} \\ \varepsilon_{\text{xc}}(\rho(\mathbf{r}), \nabla\rho(\mathbf{r})) &= \text{Exchange-correlation energy per electron as a functional of} \\ &\quad\ \rho(\mathbf{r}) \text{ and its gradient } \nabla\rho(\mathbf{r}) \end{aligned}$$

Perdew–Wang functional (PW91), Perdew–Burke–Ernzerhof functional (PBE), and PBEsol are the three most used GGA functionals, which PBEsol is more often used in densely packed solids.(Mattsson, Armiento, Schultz, & Mattsson, 2006) Other functionals such as meta-GGA and hyper-GGA are also widely used. It is very important to choose a suitable functional to better approximate Schrödinger's equation for the specific materials system of investigation. With the exchange-correlation functional specified, DFT can now solve Schrödinger's equation.

2.2.1 Standard procedure of performing DFT

DFT uses an iterative algorithm to solve the Kohn-Sham equation. First, a test electron density needs to be defined. Then, the Kohn-Sham equation is solved using the test electron density to obtain the single-particle wave function. Subsequently, the electron density determined by the Kohn-Sham single-particle wave function is calculated and compared to the electron density used when initially solving the Kohn-Sham equation. If the two densities match, the resulting electron density is considered the ground state electron density and thus can be used to calculate properties like the total energy. However, if the difference between the two densities is above certain convergence criteria, the trial electron density needs to be updated by combining the initial guess and electron density generated from the Kohn-Sham equation, and then the process gets repeated. The goal is to obtain well-converged results through this computational process which avoids directly dealing with complex many-body problems that are intrinsically unsolvable.(Sholl & Steckel, 2022)

A well-converged calculation aims to approximate the true solution of the mathematical problem as accurately as possible with the numerically derived solution by a specific exchange-correlation functional. In order to get well-numerical converged DFT calculation results, parameters such as the number of k points, energy cutoffs, and pseudopotentials need to be taken into consideration.

Firstly, the Brillouin zone (BZ) is an important concept to be considered in DFT calculations. It is the primitive unit in the reciprocal space, that is, the space of the vector k. The density of k points in the BZ affects the convergence of DFT calculations, therefore, it is very important to choose the density of k points carefully in order to obtain accurate results. In addition, when it comes to highly symmetric materials, in order to reduce the computational efforts, the irreducible Brillouin zone (IBZ) is usually considered, which is a reduced region in k-space, but it needs to be emphasized that the overall convergence of the calculation still depends on the density of k-points in the whole BZ.(Sholl & Steckel, 2022).

Secondly, energy cutoffs (E_{cut}) are often used to truncate infinite sums of solutions, thereby limiting the number of basis functions or grid points used to represent electron wave functions or densities. The choice of energy cutoff will affect the accuracy of DFT results, and the determination of the ideal value usually requires a convergence test to balance both the computational resources available and the accuracy needed. When it comes to comparing energy differences between multiple systems, it is very important to use the same energy cutoff.(Sholl & Steckel, 2022)

Next, pseudopotentials are used to reduce the computational effort caused by core electrons, which are based on the idea of using a smooth electron density to represent the density of chosen core electrons. The pseudopotential replaces the full-electron potential with an effective potential, which accounts for the screening effect of the core electrons, and aims to reduce the number of basis functions required while still providing accurate results for the property of interest. Commonly used pseudopotentials include ultrasoft pseudopotentials (USPPs) and projector augmented wave (PAW) method. Once all these parameters are specified, DFT can proceed to obtain the interested results.

In summary, DFT is a powerful first-principles calculation method that can be used to calculate the ground state properties of a system accurately. It can also be specifically used to calculate the NMR parameters and thus assist the interpretation of NMR measurement results. The employment of DFT for the calculation of NMR parameters is a powerful and efficient method for materials research as well as for understanding various material structures and properties. An enormous amount of work has been conducted before using this method to study many different types of materials, where the feasibility and reliability of this method have been demonstrated. Therefore, this thesis work also chose to employ this method to study one promising type of solid-state ionic conductor, the K-doped $CsPbF_3$ material.

2.3 General introduction of the calculation methods

All the CASTEP(Clark et al., 2005) calculations conducted in this thesis project were carried out on Delftblue(Delft High Performance Computing Centre (DHPC), 2022), the supercomputer of TU Delft. Normally three files are used for running a job, which are the .cell, .param, and the jobscript files respectively. CASTEP calculations require the presence of both the .cell and .param files, the keywords can be found in the corresponding website(*CASTEP Keywords*, 2023). While the jobscript is dedicated to the submission of the job to Delftblue. Depending on the platform used for these calculations, the exact format of the jobscript is subject to change.

The .cell file contains information regarding the unit cell or supercell, including but not limited to the lattice parameters, symmetry information, and atom positions. Extra command lines can be added here to perform extra tasks such as varying the lattice parameters or symmetry during the calculation. The k points mesh used is also indicated here. An example .cell file can be found in the appendix. The .param file consists of parameters relevant to the calculation, such as the task, the exchange-correlation functional, and the cutoff energy. It is important to set up suitable parameters here for a desired successful calculation. An example .param file is displayed in the appendix as well.

Without specifically mentioning, this thesis uses the following parameters for calculation, the PBE exchange-correlation functional, the ultrasoft pseudopotential, the Koelling-Harmon relativistic treatment, and the plane wave basis set. The calculations will generate a set of files upon finishing. Mostly the relevant information is contained in a file with a .castep suffix.

2.4 Structure exploration of $CsPbF_3$

Prior to the investigation into the K doped $CsPbF_3$, the structure information of pure $CsPbF_3$ was explored as a preparation for a better understanding of this material system. The initial cif files were obtained from The Materials Project(Jain et al., 2013), then these files can be converted to the .cell files that are used for further calculations using the cif2cell command:

```
cif2cell name-of-the-cif-file.cif -p castep --no-reduce
```

This can lead to a cell file with no reduced symmetry. Depending on the investigated materials, also considering the computational resources available, a reduced cell file according to symmetry is also used sometimes. Both the cif and cell files can be visualized in VESTA(Momma & Izumi, 2008) directly. All the plots involving crystal structures shown in this thesis are derived from VESTA. The distance between two atoms and cell volume data is also obtained from VESTA.

At the beginning of any calculations, the convergence tests are always performed to obtain the suitable k points mesh and the cutoff energy for the specific type of cell structure. To achieve this, normally three calculations would be conducted to calculate the ground state energy of the system with different sets of k-points mesh and cutoff energy. The point where the energy data starts to converge would be the optimal point. The k-points mesh and cutoff energy found here would be used as the parameter for further calculations, from the geometry optimization to the NMR calculations.

To better understand the structure information of $CsPbF_3$, several calculations were performed. Firstly, the ground state energy of the rhombohedral structure with different cell angles was compared by specifying the following command in the .cell files, which shows an example of setting the rhombohedral angle to 60.5 degrees and leaving the lattice parameter free to be optimized. The k points mesh used here is 5X5X5, and the cutoff energy is 500 eV.

```
%BLOCK LATTICE_ABC
   ANG
    6.9047495398    6.9047495398 6.9047495398
    60.500000000    60.500000000 60.500000000
```

```
%ENDBLOCK LATTICE_ABC

%BLOCK cell_constraints
      1   1   1
      0   0   0
%ENDBLOCK cell_constraints
```

Secondly, in order to explore the possible driving force behind the rhombohedral to cubic phase transition, a set of rhombohedral cells was generated with increasing lattice parameters while optimizing the lattice cell angles. The corresponding .cell files contain parameters as the following example, which is the one with lattice parameter equals 6.9 Å. The k points mesh used here is 5X5X5, and the cutoff energy is 720 eV.

```
%BLOCK LATTICE_ABC
   ANG
    6.9      6.9   6.9
    60       60    60
%ENDBLOCK LATTICE_ABC

%BLOCK cell_constraints
      0   0   0
      1   2   3
%ENDBLOCK cell_constraints
```

This could allow the lattice parameter to be fixed while three lattice angles to be optimized independently. But the resulting cells still have three angles being the same, which further proved that the rhombohedral structure is indeed more favorable for $CsPbF_3$ at 0K.

Next, to investigate the tetragonal phase change of the cubic $CsPbF_3$ upon doping K to a certain level that is mentioned in the previous literature(Wang & Ma, 2022), as well as to find whether a metastable tetragonal structure is available, the ground state energy of several tetragonal structures with different c/a ratio was calculated. The following information was written in the .cell files. The k points mesh used here for c/a = 1 would be 9X9X9, for the other c/a ratio, the k points mesh would vary according to the cell symmetry and rounded to the nearest integer, for example, for c/a = 1.1, the k point mesh used would be 9X9X8. The cutoff energy is always 720 eV.

```
%BLOCK lattice_cart
   ANG
       4.90369459156410       0.282580239096526E-08   0.805569469815663E-08
       0.282580239105604E-08  4.90369458763860       -0.305813364406164E-08
       0.805569469815663E-08 -0.305813364406164E-08   5.88443350987692
%ENDBLOCK lattice_cart

%BLOCK CELL_CONSTRAINTS
       1        1        1
       0        0        0
%ENDBLOCK CELL_CONSTRAINTS

FIX_COM : true
```

This enables the c/a ratio to be fixed at 1.2, and the exact length can be optimized while the overall structure remains tetragonal. The initial number was derived from the optimized cubic structure.

Besides the above-mentioned calculations, this project also looked into the sensitivity of CASTEP calculation when determining the ground state energy and calculating the NMR parameters with respect to different lattice parameters. The k points mesh used there is 9X9X9, and the cutoff energy is 720 eV. Some possible driving forces for the rhombohedral to cubic phase transition were also explored. These will be discussed in detail in the results and discussion section.

2.5 Supercell calculation

To investigate the influence of K atoms when they were doped into the $CsPbF_3$ system and how that contributes to the different material properties discovered, three supercells were exploited respectively. A set of relevant calculations were carried out on them as the follow-up.

2.5.1 Supercells generation and geometry optimization

Three sets of supercells were generated with the optimized cubic $CsPbF_3$ unit cell using VESTA(Momma & Izumi, 2008). Namely the 2X2X2 supercell and 2X2X1 supercell and later the 2X2X4 supercell. Then one Pb atom is replaced by a K atom for the 2X2X2 and 2X2X1 cases while two Pb atoms are replaced by two K atoms for the 2X2X4 case, for an easy reference of the atomic positions, one of the K atoms is placed at the (0,0,0) origin position for all the supercells. The 2X2X2 supercell, 2X2X1 supercell, and 2X2X4 supercell correspond to a K composition of 12.5%, 25%, and 12.5% in the K doped $CsPbF_3$ structure respectively, which can also be referred as PK12.5, PK25, PK12.5 according to the previous research.(Wang et al., 2022)

To keep the supercells still charge neutral after the doping of K atoms, one F vacancy needs to be created with one K atom introduced. For the K-doped 2X2X2 supercell, there are three F positions that have different local environments where the F vacancy can be placed, while for the 2X2X1 supercell, the number is 5. Fig 13 shows an illustration of all the F vacancy positions in the supercells, the individual positions are marked by their spatial coordinates in the crystal structures with K sitting at the origin. As for the 2X2X4 supercell, two F vacancies are formed in the supercell, and two sets of vacancy combinations with a total number being 8 are investigated, as can be visualized in Fig 19

The next step is to perform geometry optimizations for all the supercells with different F vacancy positions. The Geometryoptimization task is specified in the .param file. For the 2X2X1 supercell, the k points mesh used is 4X4X7, and the cutoff energy used is 1000 eV. For the 2X2X2 supercell, the k points mesh used is 3X3X3, and the cutoff energy used is 1000 eV. As for the 2X2X4 supercell, the k points mesh used is 2X2X1, and the cutoff energy used is 1000 eV. After geometry optimization, the ground state energy of this specific cell structure is also available in the .castep file.

2.5.2 Charge density and force vector plots

In order to better appreciate the charge density variation before and after geometry optimization for the supercells, the charge density plots were made using the method indicated in c2x(Rutter, 2018).

Two plots were made for each supercell with F vacancy, of which one was obtained using the .cell file before geometry optimization and one after. First of all, a single-point calculation was performed to generate a .check file. Next, a .cube file was produced using c2x with the following command:

```
$ c2x --cube -c name-of-the-check-file.check charge-density.cube
```

Then this cube file with a file name as charge density is visualized in VESTA. For a clearer visualization, the 2D display of the charge density was obtained. It is important to note that even though the 3D crystal structure can be sliced in any direction, it is convenient to slice it so that both the K atom and F vacancy can be visualized.

To slice, first add a new lattice plane of interest by following the path: Edit/lattice planes. Then the same plane can be sliced and displayed by the path: Utilities/2D data display. The notation here for the plane contains both the Miller index and the fractional distance from the origin. Fig 8 is an example charge density plot for the 2X2X2 supercell with F vacancy at the (0, 0, 0.25) position, the sliced plane is (100) with distance from origin equals 0.

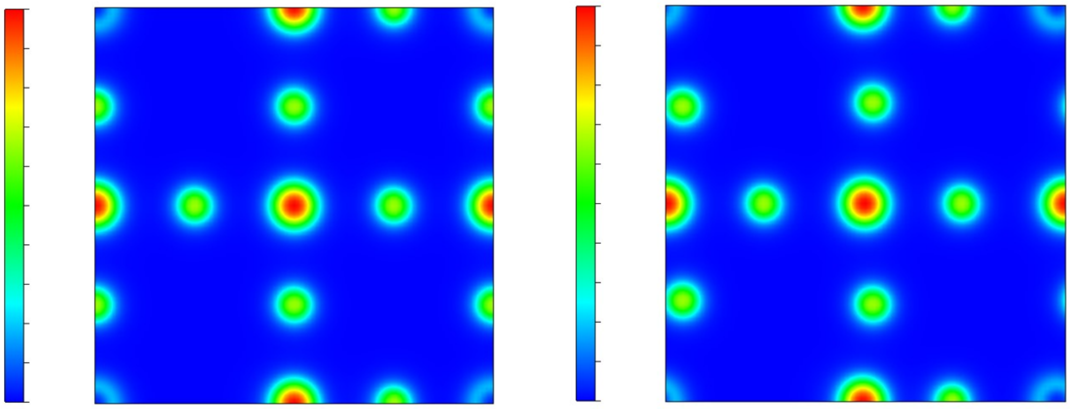

Figure 8: 2X2X2 supercell charge density plot with F vacancy at the (0, 0, 0.25) position. Sliced from the (100) plane with distance from origin equals 0. Left, before geometry optimization. Right, after geometry optimization. Green: F; Green circle with red core: Pb; purple: K; Cs atoms can not be visualized from this plot.

To analyze the forces acting on the atoms at the beginning of the geometry optimization, as well as how the atoms tend to move, the force vector plots were created. Using the forces generated in the .castep file when the calculation initiates, and the fraction of the atoms coordinates with the same order, these plots were made with Matplotlib. It is convenient to slice these plots at the plane of interest for better visualization. This can be also useful to explain the movements of atoms in the charge density plots, which will also be introduced in detail in the results and discussion section.

2.5.3 Nudged elastic band calculation

For the NEB calculations performed in this thesis project, the TRANSITIONSTATESEARCH task was used. The method was specified to NEB and eleven path points were introduced between the initial and end points. For the input cell file, besides the common position fraction block, additional product position information and one intermediate position information need to be specified. The intermediate position serves as an initial guess for the vacancy movement direction. For the calculations in the project, the intermediate points were put exactly in the middle of the two endpoints. Other relevant parameters used for NEB calculations here were referred from (Sturniolo et al., 2022) and (CASTEP Documentation, 2023). The k points mesh used for all NEB calculations performed is 3X3X3, and the cutoff energy used is 1000 eV. Upon completion of the NEB calculations, the Python script from (CASTEP Documentation, 2023) was used to analyze the result.

2.6 NMR data interpretation

For the NMR calculations performed in this thesis work, the task command in the .param file was set to Magres. The fully relaxed cell after geometry optimization is the input cell structure used here. To further test the convergence and accuracy of the NMR calculations, several additional calculations would also be performed with the number of k points mesh and cutoff energy to be slightly above or below the previously obtained results. The NMR parameters calculated will be displayed in the .castep file. Below is an example of the NMR parameters obtained from the cubic $CsPbF_3$ NMR calculation with k points mesh being 9X9X9 and cutoff energy being 720eV. Among the parameters calculated, this thesis work looked into the isotropic chemical shielding value solely.

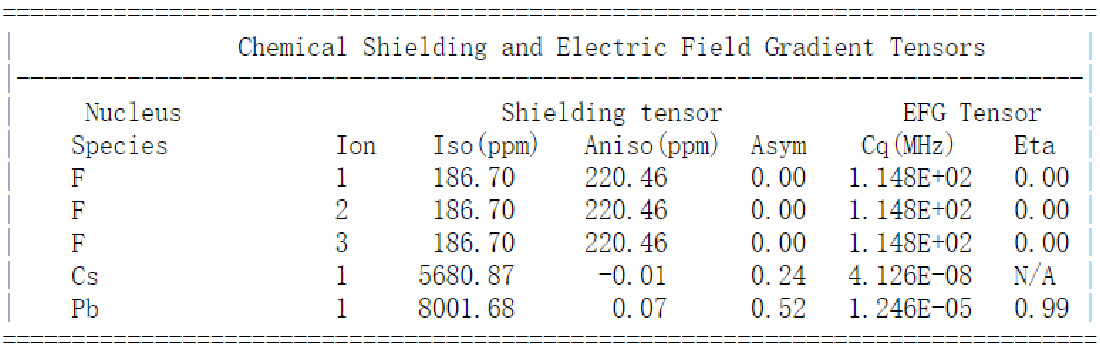

```
==========================================================================
|                Chemical Shielding and Electric Field Gradient Tensors    |
|------------------------------------------------------------------------|
|     Nucleus                     Shielding tensor            EFG Tensor  |
|    Species          Ion     Iso(ppm)   Aniso(ppm)  Asym    Cq(MHz)    Eta |
|    F                 1      186.70     220.46     0.00   1.148E+02   0.00 |
|    F                 2      186.70     220.46     0.00   1.148E+02   0.00 |
|    F                 3      186.70     220.46     0.00   1.148E+02   0.00 |
|    Cs                1     5680.87      -0.01     0.24   4.126E-08   N/A  |
|    Pb                1     8001.68       0.07     0.52   1.246E-05   0.99 |
==========================================================================
```

A .magres file will also be generated along with the NMR calculation, this file can be imported directly into the Magresview software(Sturniolo et al., 2016), where the correspondence between the σ_{iso} value and the atoms in the crystal structure can be built, the spectrum plot can also be obtained, which is helpful for the interpretation of the NMR data.

3 Results and Discussion

This chapter will introduce the elaborated results of this thesis work, followed by the interpretations and discussions of them. From the structure exploration of the pure $CsPbF_3$ material system to the investigation of the K-doped $CsPbF_3$ supercells with different numbers of atoms or K composition, the structure evolution, the forces experienced by the atoms upon doping of K, the charge density evolution of the supercells, the energy barrier of F vacancy diffusion between different positions, the calculated NMR data and their interpretations will be presented here in detail.

3.1 $CsPbF_3$ structure

$CsPbF_3$ is a material with perovskite structure while Cs sitting at the A sites and Pb is located at the B sites. It possesses several unique properties and has drawn much attention for its potential application in electrochemical or optoelectronic devices.(Murtaza et al., 2011)(Ma & Brik, 2012)(Bhumla, Gill, Sheoran, & Bhattacharya, 2021)(Roma, Marronnier, & Even, 2020) As can be seen from Fig. 9, it possesses a rhombohedral-type structure at 0K and goes through a phase transition at 187K to a cubic structure.(Yan et al., 2023) Therefore, most of the potential applications of $CsPbF_3$ focus on its cubic phase, the same case applied to the previously mentioned PK10 solid-state electrolyte.

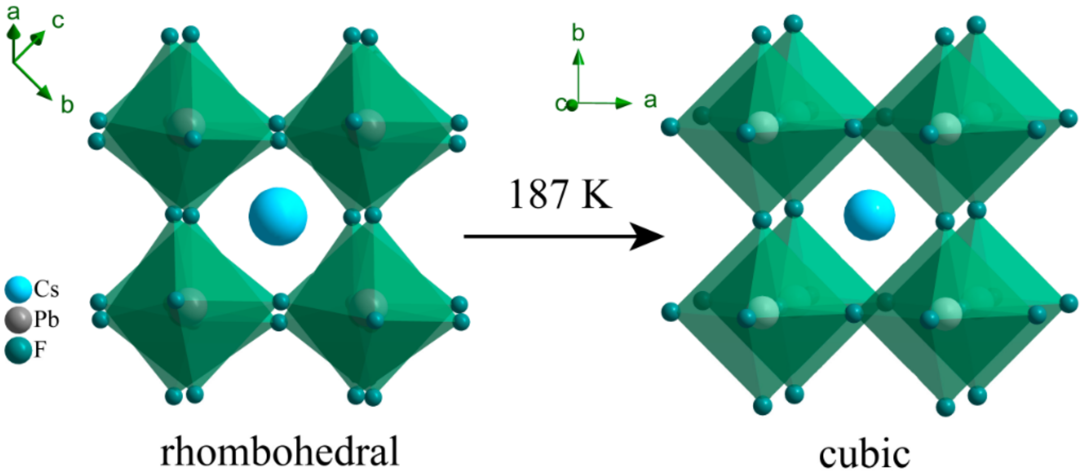

Figure 9: A transition of $CsPbF_3$ from a rhombohedral distorted perovskite structure to a cubic perovskite structure at 187 K. Retrieved from (Yan et al., 2023)

3.1.1 Evaluation of the rhombohedral structure and the rhombohedral to cubic phase trasition

To appreciate the stability of both the cubic and rhombohedral structure of the $CsPbF_3$ from an energy perspective, by considering the cubic primitive cell as a special type of rhombohedral primitive cell with cell angles equal to 60 degrees, the left part of Fig. 10 is presented. In this plot, the 0K ground state energy of seven rhombohedral cells with cell angles ranging from 60 to 63 degrees were calculated and compared. The result showed that at 0K, the rhombohedral structure is indeed more stable than the cubic structure. From this plot, it can be reasoned that the most stable structure should possess a cell angle between 60.5 and 61 degrees, which has lower ground state energy than the cubic structure with a cell angle being 60. The results here are slightly different from what has been presented by The Materials Project(*Materials Project*, 2023), where the most stable structure has a cell angle equal to 62.29 degrees. The inconsistency could be attributed to the different exchange-correlation functionals used in the calculations, with PBE for this work and r2SCAN metaGGA functional for The Materials Project. Other different parameters used for calculations could also lead to this difference, but the overall trend observed by the two studies is comparable and the calculated energy difference between the cubic and rhombohedral structures is small according to both studies.

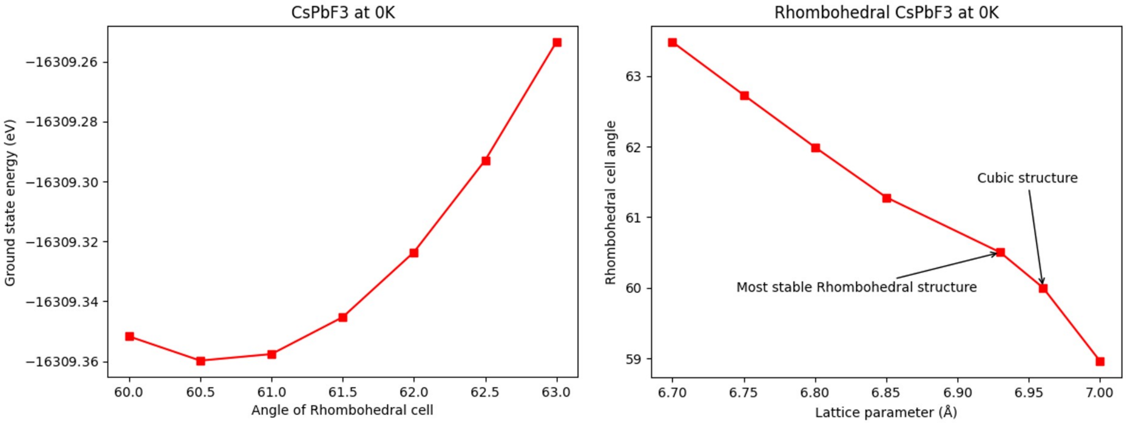

Figure 10: Left: Ground state energy at 0 K of $CsPbF_3$ rhombohedral structure unit cells with cell angles ranging from 60 to 63 degrees. The unit cells used here contain two formula units of $CsPbF_3$. Right: Correlations between the optimized cell angle and different lattice parameters induced for the rhombohedral $CsPbF_3$ structure at 0K.

Since the cubic $CsPbF_3$ structure corresponds to the most stable structure at room temperature, which is also the structure observed with the most pronounced F ion conductivity, taking the larger number of k points that could be potentially incorporated for calculations with cubic symmetry into account as well, for the further study carried out in this thesis, the cubic $CsPbF_3$ structure is the focus. It will also be used to generate the supercells that are essential for the further research of this thesis project, thus a good understanding of the cubic structure is of vital importance. A primitive study is carried out here to investigate the possible driving forces for this rhombohedral to cubic phase transition at 187K.(Yan et al., 2023) As can be seen from the right part of Fig. 10, with the lattice parameter increasing, the optimized lattice angle of the rhombohedral cell tends to decrease. Hence, one can argue that due to the lattice expansion at a higher temperature, the most stable structure will have a lower lattice angle preferred. At a certain temperature, the preferred angle could turn to be exactly 60 degrees, thus forming a cubic structure. It is worth noting that why the material remains to possess a cubic structure at a temperature higher than 187K is hard to explain with this argument, and the exact reason might be multifaceted, other effects could also play an even more dominant role in this phase change, such as the entropy difference between the cubic and rhombohedral structure, with the cubic $CsPbF_3$ being the one with higher entropy.

It is important to note here that the presence of the Pb lone pair could also make a difference in this case, previous studies have also researched this deeply and mentioned some special properties that could possibly be introduced by the Pb lone pair. For example, with $CsPbF_3$ being the only ABF_3 type perovskite material with a polar ground state that has been synthesized experimentally, Smith et al.(Smith, Benedek, & Fennie, 2015) studied the interactions between lone pairs, octahedral rotations, and A or B site driven ferroelectricity. They found that the lone pair from the B site cations stabilizes the polar ground state, which is different from the oxide perovskite materials, where the A site cations are responsible. They also found that the lone pair could influence the lowest energy structure by determining the nonpolar structural distortion pattern or the PbF_6 octahedral rotations. Additionally, Li et al.(L. Li et al., 2022) revealed that for post-transition metal halides, the energy difference between the cation s-state and the halogen p-state can determine the degree of the stereochemical activity of the lone pairs, which showed that metal halides can also be studied by using the same revised model regarding the stereochemical activity of lone pairs of the metal oxides.

3.1.2 Evaluation of the cubic structure and the cubic to tetragonal phase transition

Next, geometry optimization was performed on the cubic structure with Castep to obtain the relaxed cubic unit cell. The optimized cell has a lattice parameter equal to 4.90 Å, which also exhibited a slight inconsistency with the value found on The Materials Project being 4.83 Å. This is likely to be induced by the same reason mentioned previously, for instance, the different exchange-correlation functionals used. It is worth noting that the lattice parameter obtained experimentally for cubic $CsPbF_3$ is 4.80 Å,(Wang et al., 2022) this could offer a rough suggestion of the accuracy here. To better appreciate the accuracy and sensitivity of both the geometry optimization and the further NMR calculation using Castep, the ground state energy and isotropic chemical shielding value were calculated and plotted here for a set of cubic unit cells with different lattice parameters ranging from 4.75 Å to 4.95 Å. As can be visualized in Fig. 11, this calculation method is capable of searching for the lattice parameter with the lowest ground state energy and thus finding the most stable structure. It can also well distinguish the isotropic chemical shielding value from slightly different structures.

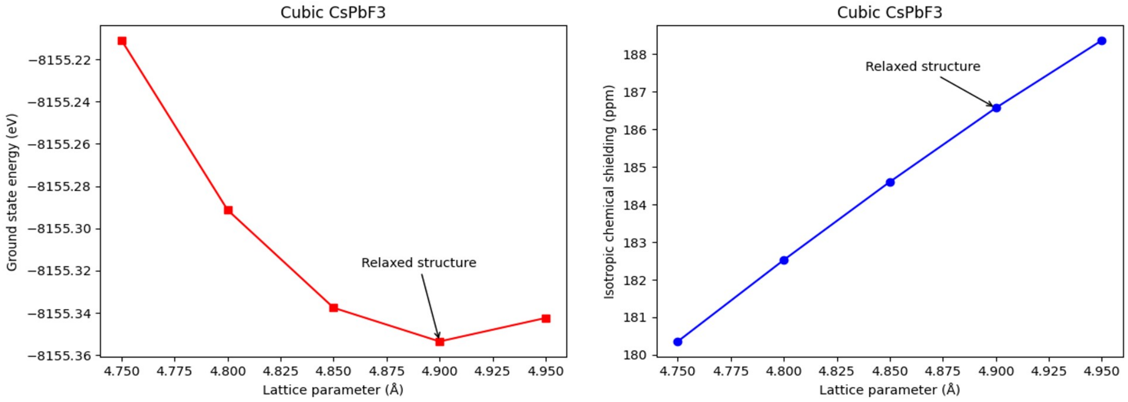

Figure 11: Correlations between the ground state energy (left) and isotropic chemical shielding (right) with lattice parameter changing from 4.75-4.95 Å in the Cubic $CsPbF_3$ structure. The data for the optimized structure is indicated specifically.

The previously mentioned research has already revealed that upon doping K atoms into the $CsPbF_3$ to a certain level, the materials will go through a phase transition from cubic structure to tetragonal structure, with the preferred c/a ratio smaller than 1.(Wang & Ma,

2022) To explore the driving force behind this phase change as well as to understand the relations between the cubic $CsPbF_3$ and tetragonal $CsPbF_3$, the ground state energy and isotropic chemical shielding data of a set of tetragonal cells with c/a ratio ranging from 0.8 to 1.2 were calculated, as in Fig. 12. The idea for this calculation is to find out whether a tetragonal $CsPbF_3$ with a certain c/a ratio is more energetically favorable than other structures with different c/a ratios or even more stable than the cubic structure. If this is the case, then the presence of this structure could provide the driving force for the phase transition upon doping K. From the left part of Fig. 12, no local minima were observed except the cubic structure. Within the c/a ratio between 0.8 and 1.2, the closer the value to 1, the more stable the structure will be. It is interesting to note that when the c/a ratio shifts the same magnitude, the structure becomes even less stable when contracting along the c direction compared to the expansion case where c/a is larger than 1. This set of calculations further proved the cubic structure to be more energetically favorable than tetragonal structures in the given c/a ratio range for pure $CsPbF_3$. However, the ground state energy for structures with a c/a ratio closer to 1 but not equally is relatively similar to the cubic structure. This could be interpreted as an inclination for phase transitions especially when external atoms are introduced into the system.

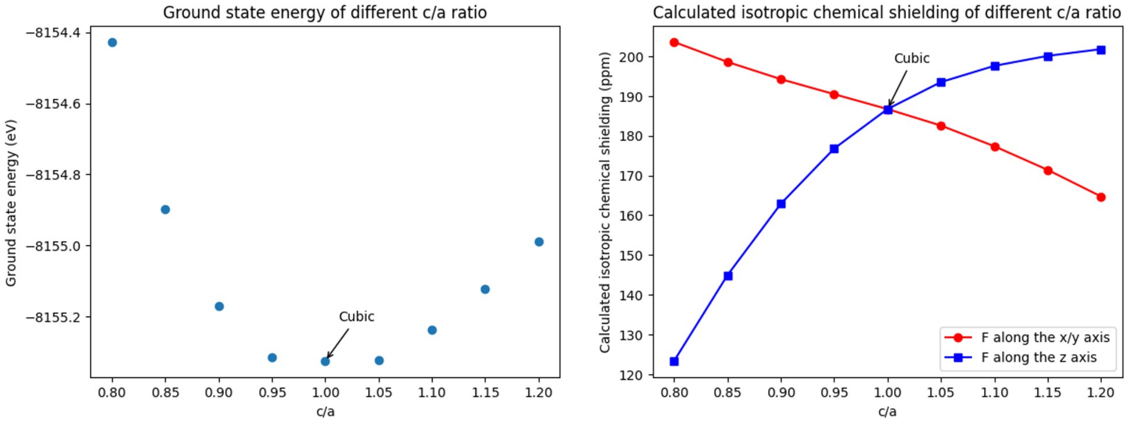

Figure 12: Tetragonal $CsPbF_3$ with c/a ratio varying from 0.8 to 1.2 with respect to left: ground state energy with 1 formula unit of $CsPbF_3$; right: calculated isotropic chemical shielding value. The cubic structure which has a c/a ratio equal to 1 is pointed out specifically.

3.1.3 Calculation and rationalization of the chemical shielding trends for tetragonal distortion

The calculated isotropic chemical shielding data in the right half of Fig. 12 shows two distinct lines. In this case, one formula unit of $CsPbF_3$ contains three F atoms, two of them have the same isotropic chemical shielding value and the other has a different one in the tetragonal structure with a c/a ratio non-equal to one. This can be explained by the appearance of two distinct F atoms' local environments in the tetragonal structure. The F atoms along the x and y-axis have the same chemical environment while those along the z-axis have another local environment, the ratio of x- and y-F atoms together to z-F atoms is exactly 2:1.

To rationalize the change of the isotropic chemical shielding data with respect to the c/a ratio. The first hypothesis proposed here is to connect this with the Pb-F distance, since the closer the F atoms are to the Pb atoms, the more shielding they will experience, resulting in a large σ_{iso} value. As can be seen in Table. 1, the trend here does not match the hypothesis. With the c/a ratio increasing, on the one hand, the distance between those F atoms along the x or y-axis and the neighboring Pb atoms decreases which means a higher shielding for the F atoms from these Pb atoms, but from the calculations, the isotropic chemical shielding data is decreasing as well, which corresponds to a declined electron density around these F atoms, these two do not agree with each other. On the other hand, the F atoms on the z-axis will experience an increasing distance from their neighboring Pb atoms with the increasing c/a ratio. Since Fig. 12 shows an increasing isotropic chemical shielding value for z-F atoms, which means the electron density around those F atoms is increasing, this does not match with the F-Pb distance again.

One can now argue whether the Cs-F distances can play a role in this case. If we check the data from the table, we can see the x/yF-Cs distance first decreases and then increases, which unfortunately does not match the trend again. While for the zF-Cs distances, they decrease with the c/a ratio increasing which is in line with the calculated trend for σ_{iso} value. The cell volume change regarding the c/a ratio also exhibits a decreasing then increasing pattern, it is hard to link this to the σ_{iso} trend straightforwardly as well. Until this point, no clear hypothesis has been established yet to successfully explain the variation of the σ_{iso} value. It is important to point out that the isotropic chemical shielding value is influenced by the overall electron density felt by the specific atoms, the neighboring cation-F distances interpretations here can only serve as a hypothesis for characterization and appreciation purposes. The exact reason could be complicated, for example, the second closest Pb atoms of the F atoms could also make a non-negligible difference.

Table 1: Cell volume change and the F-(neighboring) cation distances of the tetragonal $CsPbF_3$ structures with c/a ratio ranging from 0.8 to 1.2

c/a ratio	Cell volume (Å^3)	(x/y)F-Cs distance (Å)	(x/y)F-Pb(Neighbor) distance (Å)	(z)F-Cs distance (Å)	(z)F-Pb distance (Å)
0.8	130.24	3.5	2.73	3.86	2.18
0.85	124.03	3.45	2.63	3.72	2.24
0.9	120.22	3.44	2.56	3.61	2.3
0.95	118.23	3.44	2.5	3.53	2.37
1	117.92	3.47	2.45	3.47	2.45
1.05	118.72	3.51	2.42	3.42	2.54
1.1	120.13	3.55	2.39	3.38	2.63
1.15	122.26	3.61	2.37	3.35	2.72
1.2	124.97	3.67	2.35	3.33	2.82

3.2 K doped $CsPbF_3$ material

From this section, the K doped $CsPbF_3$ will be the focus. To study the materials with different K compositions, a set of supercells are created and investigated.

3.2.1 Goldschmidt tolerance factor

The Goldschmidt tolerance factor(Megaw, 1946) is an often used parameter to indicate the crystal structure and stability of perovskite materials. It can be calculated with the following equation:

$$t_G = \frac{r_A + r_X}{\sqrt{2}(r_B + r_X)}, \tag{8}$$

where:

r_A : radius of the A-site cation,
r_B : radius of the B-site cation,
r_X : radius of the anion.

Generally speaking, when the t_G value is between 0.9 and 1.0, the material tends to have a cubic structure. A t_G value between 0.71 and 0.9 would result in a distorted perovskite structure with tilted octahedra. If the t_G value is smaller than 0.71 or larger than 1 then a perovskite structure would not be preferred anymore.(Z. Li et al., 2016)

For the K doped $CsPbF_3$ case, the ionic radius with specific charge and coordination number are presented in Table. 2. The Goldschmidt tolerance factor calculated with these numbers for pure $CsPbF_3$ is 0.9, which indicates that the $CsPbF_3$ is right at the edge of taking a cubic perovskite structure. Since the ionic radii of K^+ are smaller than Cs^+ while larger than Pb^{2+} in this case, one can argue that no matter which atom the K^+ will replace, Cs or Pb, no matter where the K atom will locate at, the A or B site, the consequence of doping K^+ will always be a smaller t_G value for the material, which leads to a distorted perovskite structure with tilted octahedra. To put it more specifically, if all Cs were replaced by K, the t_G value would be 0.76. If it is all the Pb atoms are replaced by K, the t_G value would be 0.84 instead.

Table 2: Ionic radius in the K doped $CsPbF_3$ materials system with specific charge and coordination number. Retrieved from (Shannon, 1976)

$Ions^{charge}$ (coordination number)	K^+ (VI)	Cs^+ (XII)	Pb^{2+} (VI)	F^- (VI)
Ionic Radii (Å)	1.38	1.88	1.19	1.33

3.2.2 Supercells generation and structure optimization

In the previous research carried out on the K-doped $CsPbF_3$ material, the researchers suggest that K will most likely replace the Pb atoms and form an F vacancy at the same time thus contributing to a high F^- ion conductivity.(Wang et al., 2022) In this thesis work, this suggestion is followed to build the supercells using one K atom to replace one Pb atom in one supercell and form one F vacancy at the same time. Two supercells were created based on the fully relaxed cubic $CsPbF_3$ unit cell, with one being the 2X2X1 supercell corresponding to a K composition of 25% and the other being the 2X2X2 supercell corresponding to a K composition equals 12.5%. Using the same notation as in the previous paper, these two supercells can also be referred to as PK25 and PK12.5 respectively.(Wang et al., 2022) Since the previous study also revealed a phase transition of this material system from cubic to tetragonal with a K composition in between 10-15%(Wang & Ma, 2022), also considering the computational resources, these two supercells could serve as a good starting point to probe into the phase structure and properties of this specific material of interests.

Upon one K atom being aliovalently doped into the $CsPbF_3$, one F vacancy needs to be generated accordingly to balance the charge of the material system. As for where the F vacancy should be located, there is more than one possible position for the F vacancy to sit. As a matter of fact, three positions are available for PK 12.5 while five positions are available for PK25, as indicated in Fig. 13. For the PK12.5 case, position 1 is directly connected to the doped K atom, position 2 is connected to the closest Pb atom of the doped K, and position 3 is connected to the second closest Pb atom of the K atom. As for the PK25 case, positions 1 and 2 are both directly connected to the doped K and have the same distance to K but with different local environments, with position 1 in between two K and position 2 in between one Pb and one K. The same scenario also applies to position 3 and position 4 here, they are both connected to the closed Pb atom of the doped K but position 3 has two closest K atoms, while position 4 has four closest K atoms. Position 5 in PK25 is comparable with position 3 in PK12.5, being connected to the second closest Pb atom of the doped K.

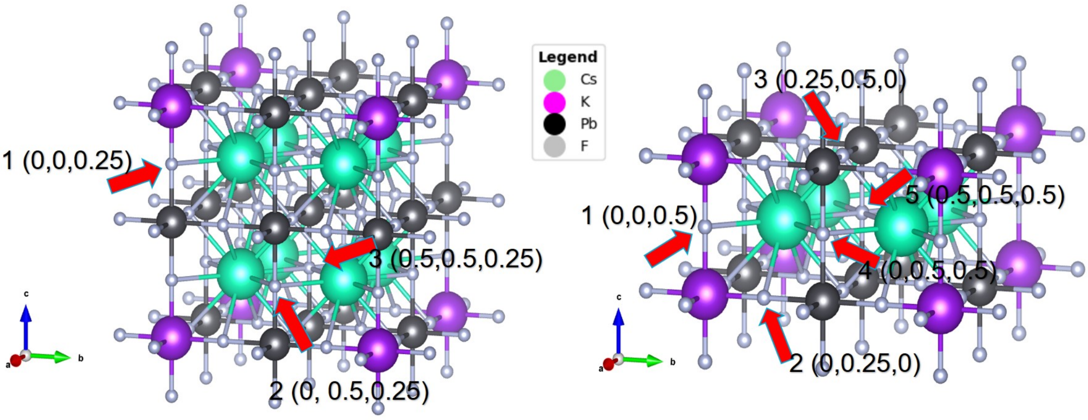

Figure 13: K doped $CsPbF_3$ supercells with one Pb atom replaced by one K atom in each case, the K atom located at the origin position. Left: 2X2X2 supercell, PK12.5. Right: 2X2X1 supercell, PK25. Possible F vacancy positions upon the doping of the K atom are indicated with the red arrow, the notation and fractional coordinates of these positions are also listed for each supercell respectively. The crystal structure is visualized and retrieved using VESTA(Momma & Izumi, 2008).

Supercells with all these eight possible F vacancy positions mentioned above were generated and relaxed as the first step. The lattice parameter change and cell volume change are tracked and recorded in Table. 3 and Table. 4 respectively. Some general trends can be observed here from these data. Firstly, the relaxed cells do not have a cubic symmetry anymore. Secondly, the supercells experience a cell volume expansion for all the cases tested here except position 2 in the 2X2X1 supercell. One can expect that this expansion is induced by a local expansion around the F vacancy in the relaxed cell, the expansion observed here is different from what has been observed experimentally in the previous research where they mentioned a decreased cell volume upon doping K atoms(Wang & Ma, 2022). Thirdly, the closer the F vacancy is to the doped K atom, the lower the expansion

Table 3: The lattice parameter change of the two supercells after geometry optimization for F vacancy at different positions. The lattice parameter is normalized and displayed as one cubic unit cell.

Material system	Position	Original lattice parameter of the cubic unit cell (Å)	Optimized lattice parameter of one unit cell (ÅXÅXÅ)
2X2X2 supercell	1	4.90	4.90X4.89X4.92
	2	4.90	4.92X4.93X4.89
	3	4.90	4.92X4.92X4.90
2X2X1 supercell	1	4.90	4.94X4.94X4.85
	2	4.90	4.90X4.95X4.86
	3	4.90	4.89X4.97X4.91
	4	4.90	4.92X4.97X4.91
	5	4.90	4.95X4.95X4.91

rate of the supercell volume will be. Fourthly, by comparing two supercells, it reveals that with a higher K composition, the cells tend to change more as a consequence. Last but not least, despite the apparent lack of correlation between the changes in lattice parameters and different F vacancy positions relative to the K site, a rationalization of these observations and detailed analysis can still be presented, which will be discussed in detail later in separate sections.

Table 4: The cell volume change of the two supercells after geometry optimization for F vacancy at different positions.

Material system	Position	Original cell volume ($Å^3$)	Optimized cell volume ($Å^3$)	Volume expansion ($Å^3$)	Volume expansion rate (%)
2X2X2 supercell	1	943.32	943.78	0.46	0.049
	2	943.32	947.93	4.61	0.49
	3	943.32	949.42	6.1	0.65
2X2X1 supercell	1	471.66	473.71	2.05	0.43
	2	471.66	470.08	-1.58	-0.33
	3	471.66	477.55	5.89	1.25
	4	471.66	480.72	9.06	1.92
	5	471.66	481.47	9.81	2.08

3.2.3 Ground state energy calculations

After performing the geometry optimization for all the supercells, the ground state energy for the fully relaxed cells is recorded and studied. The energy data with the F vacancy at different possible positions are shown in Fig 14 below.

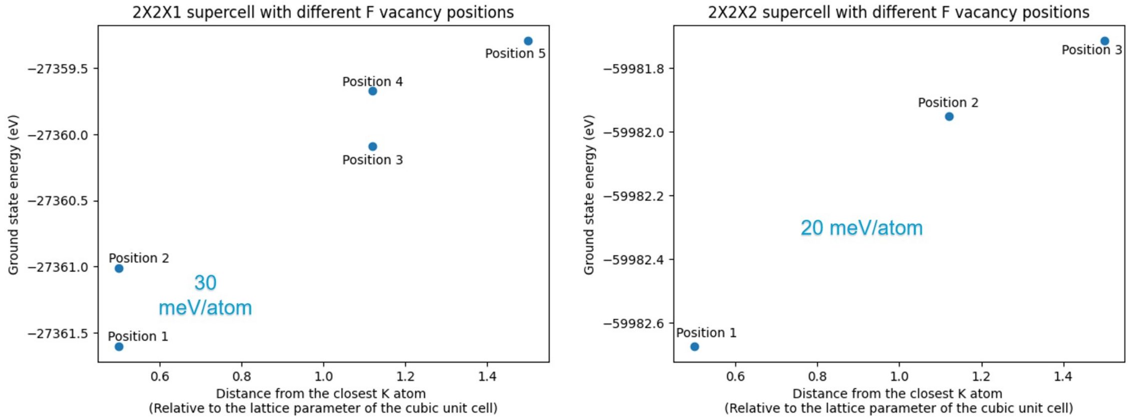

Figure 14: Ground state energy of the 2X2X1(Left) and 2X2X2(Right) supercells with respect to the different positions for the one F vacancy in one supercell. The x-axis represents the distances from the F vacancy to its closet K atoms with the lattice parameter of the original $CsPbF_3$ cubic unit cell being one. The y-axis shows the ground state energy. The energy difference per atom between position 1 and position 2 for both supercells is specifically marked.

According to this figure, several general trends can be observed. Firstly, the smaller the distance between the F vacancy and the doped K atom, the lower the ground state energy of the structure will be thus making the K-doped $CsPbF_3$ system more stable. Secondly, for the 2X2X1 supercell, comparing position 1 and position 2 which have the same $K - V_F$ distances, it can be seen that when the F vacancy is in between two K atoms, the system is more stable than the case when F vacancy is in between one K and one Pb atoms. Similarly, by comparing position 3 and position 4, it can be observed that position 3 has a lower energy which may be linked to a smaller number of closest K atoms. Last but not least, the energy difference between position 1 and position 2 of the 2X2X1 supercell is about 600 meV, which corresponds to around 30 meV per atom. The energy difference between position 1 and position 2 of the 2X2X2 supercell is about 720 meV, which corresponds to around 20 meV per atom. This could suggest that the ground state energy difference is less significant between position 1 and position 2 in both supercells with room temperature corresponding to 25 meV per atom, which could facilitate the hopping of F vacancies in the crystal structure thus contributing to a high F ion conductivity, but the exact energy barrier and energy landscapes need to be further investigated in order to conclude this, which will be discussed specifically in the NEB calculation section later.

3.2.4 Supercells charge density and forces investigation

To appreciate the charge density of the atoms in the material, especially for the Pb atoms, and to see the charge density variations before and after the geometry optimization, and also to check whether the presence of the Pb lone pair could influence its local structure, the charge density plots both before and after geometry optimization are generated. Fig 15 shows the example of the 2X2X1 supercell with F vacancy located at position 3. For a clearer visualization, the plot is sliced at the plain where the F vacancy is located and displayed in 2D. In this example, it is sliced at the (001) plane with a distance to the origin equal to zero. Moreover, in order to visualize the forces applied to the atoms in the supercells and understand why the atoms tend to move in these specific ways that lead to the optimized cell structure, the force vectors are also plotted here together with the charge density plot using the force components generated when initiating the geometry optimization. For a clearer visualization, this plot is also sliced at the same plane as in the charge density plot.

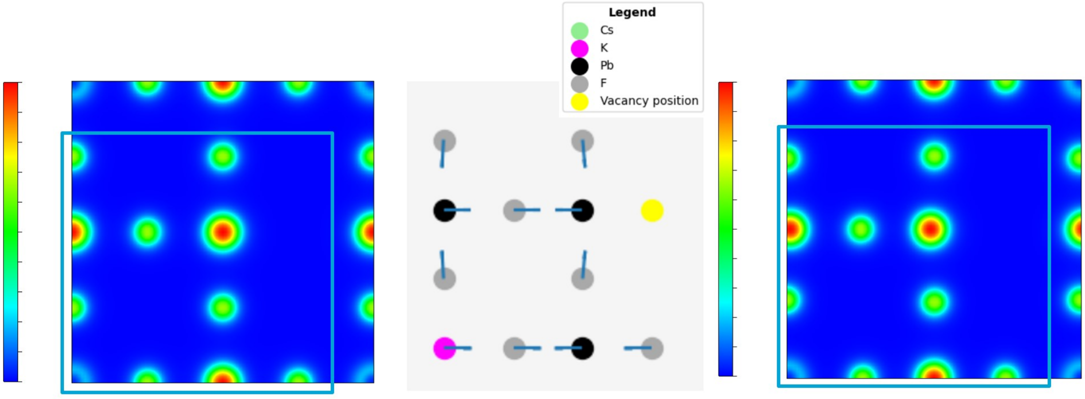

Figure 15: The charge density plots for the 2X2X1 supercell with F vacancy at position 3 before(Left) and after(Right) the geometry optimization. The plot shows the forces applied to all atoms when initiating the structure optimization(Middle). All three plots are sliced at the (001) plane with the distance to the origin equal to 0. The color scale for the charge density demonstrates that red is the highest and dark blue is the lowest. The F vacancy position is marked with a red arrow in the first charge density plot. The exact part corresponding to the force vector is indicated in the charge density plots with a frame for clear comparison. The force vectors in the middle plot are the 2D projection on this plane and are shown on the same scale.

Several findings can be observed here according to Fig 15. Firstly, the charge density plot after geometry optimization successfully exhibits some structural information such as the local distortion of the Pb octahedral, which agrees with what can be seen from the structure. This proves the credibility of the charge density plot to a certain degree. Secondly, the charge density near the Pb atoms is a uniform sphere, which is different from the previous expectation. The presence of the lone pair of Pb was expected to create polarisation for the charge density around the Pb atoms and thus resulting in a local distortion of the Pb octahedral. This can not be observed from either the charge density plot prior to the geometry optimization or after, despite that a local distortion of the Pb octahedral is indeed presented. The study by Walsh and Watson(Walsh & Watson, 2005) suggested that the anion-cation interactions are actually the reason for the asymmetric electron density, which is also connected with the formation of distorted structure and the presence of lone pair activity. This could provide a possible direction for further investigating the findings mentioned above.

Next, with the appearance of the excess F vacancy, the resulting composite quantum objects can be recognized as polarons.(Franchini, Reticcioli, Setvin, & Diebold, 2021) As for the directions of the forces in the force vector plot, they can be explained by the coulombic interaction, with F vacancy having an effective positive charge thus repelling its neighboring Pb atoms while attracting the F atoms, and the doped K atom having an effective negative charge thus repelling its neighboring F atoms while attracting the other metal atoms in general. This force plot could also explain the variation of the charge density before and after geometry optimization for this case specifically with the F vacancy located at position 3 in the 2X2X1 supercell.

3.3 Structure distortion analysis and NMR parameters interpretation of the cell with 25% K composition (2x2x1 supercell)

This section will discuss the findings from the calculations of different F vacancy positions in the 2X2X1 supercell, aka PK25, and offer explanations for those findings case by case according to the different F vacancy positions, from the optimized structure to the interpretation of its calculated NMR parameters. Since for the 2X2X1 supercell, planes contain the B position cations stacked continuously along the c direction, the plane stress condition could be used in this case to rationalize the structure distortions and elastic deformations observed. The cation-vacancy-cation vectors in each case will also be considered to explain the findings, this will be written as B-V-B, for example, Pb-V-K vector.

3.3.1 Position 1

When the F vacancy is located at position 1 in the 2X2X1 supercell, a series of K-V-K vectors is presented and connected with each other forming a continuous chain along the z-axis, while it is symmetrical between the x and y axes. It can be expected that the changes are identical along the a and b directions. From Table. 3 and Table. 4, it can be seen that this is indeed the case. The cell volume experiences a 0.43% expansion, specifically a contraction along the c direction while a symmetric expansion along the a and b direction. This is different from the previous perception that a local expansion is presented around the F vacancy. This could be rationalized by the fact that the F vacancy has an effective positive charge while the doped K atom has an effective negative charge thus they attract each other and contribute to the contraction along the c direction.

For the NMR calculation, it can be seen from Fig 16 that there are three different sets of values for the F atom isotropic chemical shielding in the optimized cell. The F atoms connected to K atoms have the highest σ_{iso}, corresponding to a high shielding experienced. The rest F atoms that are in between one Pb and one K have lower and close σ_{iso}.

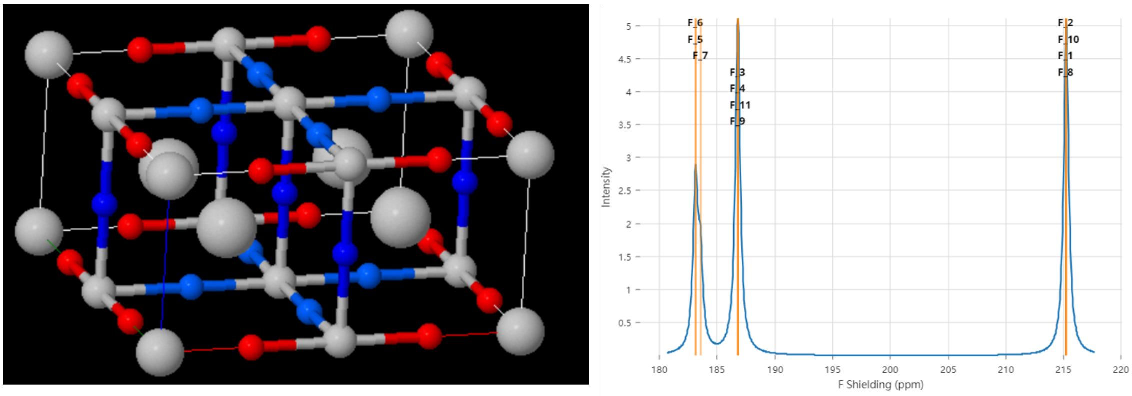

Figure 16: Visualization of the calculated isotropic chemical shielding data for the 2X2X1 supercell with F vacancy located at position 1. Left: the σ_{iso} for each individual F atom displayed in a color scale, with red being the one with the highest value and dark blue being the one with the lowest. Right: the σ_{iso} data for all F atoms showed in the spectrum form. Visualized using MagresView(Sturniolo et al., 2016)

3.3.2 Position 2

When the F vacancy is located at position 2, the Pb-V-K vectors will form along the x- or y-axis, and the vectors do not connect with each other which means no B-V-B-V-B chains are available in this case. The vectors along the a direction are investigated here as an example. Under this circumstance, the cell contracts by 0.33%, while the lattice parameter along the a direction is relatively unchanged and an expansion along the b direction and a contraction along the c direction can be observed. One can argue that in this case, the B-V-B vector direction will remain relatively fixed while the direction perpendicular to it would expand except for the c direction where a contraction happened on the contrary. This might be again linked to the coulombic forces felt by the atoms due to the non-neutral effective charges in the crystal structure.

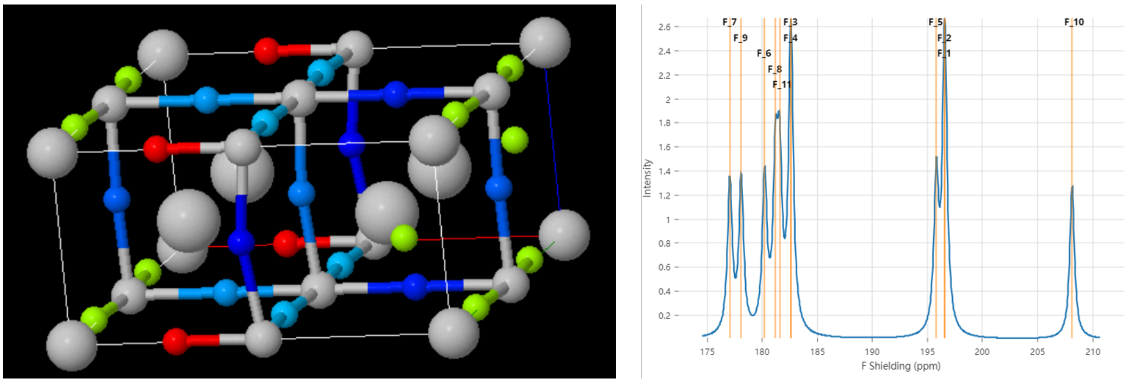

Figure 17: Visualization of the calculated isotropic chemical shielding data for the 2X2X1 supercell with F vacancy located at position 2. Left: the σ_{iso} for each individual F atom displayed in a color scale, with red being the one with the highest value and dark blue being the one with the lowest. Right: the σ_{iso} data for all F atoms showed in the spectrum form. Visualized using MagresView(Sturniolo et al., 2016)

From the NMR calculation for this case showed in Fig 17, the F atoms with the highest σ_{iso} are also located in between a K and a Pb atom. But for the rest of F atoms, the σ_{iso} value is widely scrambled, no clear trends can be observed here straightforwardly. Unfortunately, the same confusing data is presented for the position 3,4 and 5 cases in the 2X2X1 supercell, the corresponding figures are provided in the appendix for reference without further discussion on them in this section.

3.3.3 Position 3

For the case where F vacancy sits at position 3, a series of Pb-V-Pb vectors will form either along the a or b direction, the example examined here is for the vectors along the a direction. The vectors in this supercell do not connect with each other and therefore no infinite B-V-B-V-B chains are available here as well, making it comparable to the previous position 2 case with the difference being no K atoms directly connected to the vacancy. The cell volume expands by 1.25% here. The a lattice vector slightly contracts and the b lattice vector obviously expands compared to the slight expansion of the c lattice vector. When comparing this case to the position 2 case, it can be seen that the B-V-B direction does not change much, and on the b direction which is perpendicular to the vector direction, considerable expansion can be observed. The difference lies in that for position 2, the c direction contracts while it slightly expands for the position 3 case here. To explain what has been found, first of all, it can be seen from the relaxed structure that the Cs atoms only move along the ab plane, this further indicates that the plane stress condition can be applied here, also considering the periodic boundary condition, it is explainable for the structure to expand along the ab plane. But how to explain the finding that the expansion is mainly concentrated on the b direction being perpendicular to the B-V-B vectors and why different trends happened for position 2 and 3 cases along the c direction is still unclear at this moment.

3.3.4 Position 4

In the position 4 case, Pb-V-Pb vectors are formed along the z-axis, and these vectors can connect with each other to build a continuous chain along the c direction. The cell volume expands by 1.92% and expansion along all three directions. The expansion is mainly concentrated in the b direction as well and changes along the a and c directions are rather small. This case is comparable to the position 1 case with the difference that here the vector is Pb-V-Pb instead of K-V-K, this could help to explain the expansion along the c direction instead of contraction similar to the position 1 case, with the lacking of coulombic attractions between cations and vacancies. Also unlike the position 1 case, the a and b directions here are not symmetrical. The Pb-Pb plane is along the a direction and incorporates the Pb-V-Pb infinite chains while the b direction is the Pb-K planes instead. This could be potentially used to argue the difference in terms of lattice expansion with the Pb-K plane being more favorable to significant changes.

3.3.5 Position 5

When the vacancy is located at position 5, an infinite chain of Pb-V-Pb vectors will also be formed along the c direction. Unlike the previous position 4 case, the structure here is symmetric between the a and b directions. This is indeed the case according to the relaxed structure. The cell volume expands by 2.08% which is the largest among all five positions, with the same degree of expansion along the a and b directions, and relatively small expansion along the c direction. The slight expansion along the c direction is similar to the position 4 case and therefore can be rationalized by the same hypothesis. It is worth noting that when comparing the expansion along the a and b directions for both the position 4 and 5 cases, the Cs atoms here could also make a difference, as the difficulties for them to move towards the Pb-Pb plane or Pb-K plane are different considering the difference between Cs-Pb and Cs-K interactions.

3.4 Structure distortion analysis and NMR parameters interpretation of the cell with 12.5% K composition (2x2x2 supercell)

Similarly to the previous section, this section will also discuss the findings from the calculations regarding different F vacancy positions in the 2X2X2 supercell, aka PK12.5, and offer explanations for those findings from the relaxed structure to the interpretation of its NMR parameters. The plane stress condition can also be applied here and the cation-vacancy-cation vectors are also used to explain the findings. Generally speaking, the change in terms of the cell volume or the lattice parameters is less compared to the 2X2X1 supercell, this could be potentially linked to the low K composition here.

3.4.1 Position 1

When the F vacancy is located at position 1 in the 2X2X2 supercell, Pb-V-K vectors would form without the creation of a continuous chain. The example investigated here is for the vectors along the z-axis, one could expect the change in the a and b direction would be symmetric. In this case, the cell volume expands by 0.049%, and the lattice parameter does not change much along the a direction, while slight contraction along the b direction and slight expansion along the c direction are observed. This does not agree with the previous assumption but considering that the volume change here is relatively small compared to other cases, it is less convincing to draw a conclusion here.

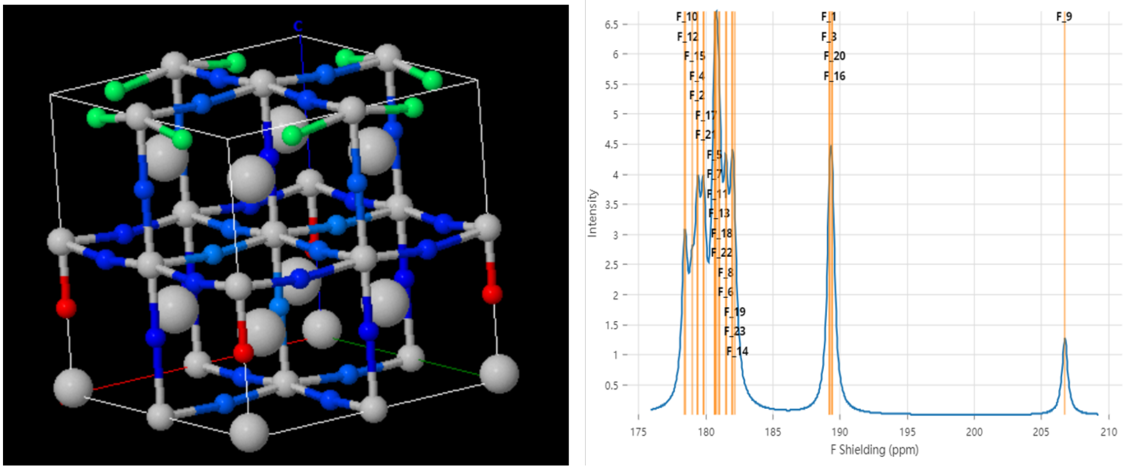

Figure 18: Visualization of the calculated isotropic chemical shielding data for the 2X2X2 supercell with F vacancy locates at position 1. Left: the σ_{iso} for each individual F atom displayed in a color scale, with red being the one with the highest value and dark blue being the one with the lowest. Right: the σ_{iso} data for all F atoms showed in the spectrum form. Visualized using MagresView(Sturniolo et al., 2016)

From the NMR calculation for this case shown in Fig 18, it can be observed that the F atoms connected to the vacancy connecting Pb atoms exhibit the highest σ_{iso}. This could be rationalized by the coulombic forces induced by the vacancy on Pb, by pushing the Pb atoms to the F atoms on the other side, it can contribute to a high shielding. Since the F-cation distances are also scrambled in this case, it is hard to say which cation would be more influential on the σ_{iso} of the F atoms. The σ_{iso} for other F atoms in this case also cannot be categorized and rationalized at this moment. Similar to the 2X2X1 supercell, the calculated NMR result also gets more complex with the F vacancy position number going higher. The position 2 and 3 cases will not be further discussed here, the extra figures are available in the appendix.

3.4.2 Position 2

For the case where F vacancy is located at position 2, the Pb-V-Pb vectors can form along any direction without continuous chains forming. The example used here is also for vectors along the z-axis. Unlike the previous position 1 case, the a and b directions are not symmetric. This is supported by the data from the optimized cell, where the volume expands by 0.49% and different degrees of expansion are experienced for the a and b directions and slight contraction for the c direction. What shows here is different from the position 4 case in the 2X2X1 supercell where the c direction undergoes expansion. One could argue according to this that a continuous B-V-B chain could cause the lattice to expand along the chain direction while if no chains are available, just some vectors stagger along the same direction, it would lead to a contraction instead.

3.4.3 Position 3

For the position 3 case of the 2X2X2 supercell, similarly to the previous position 2 case, the Pb-V-Pb vectors will be created without connecting with each other, so still no chains are present. But here one can expect the symmetry along the other two directions. The example investigated here is still along the z-axis. The cell volume expands by 0.65% and symmetrical expansion along the a and b directions is observed indeed. The c direction remains rather fixed in this case, which is different from the position 5 case in the 2X2X1 supercell. Therefore, when taking the position 2 and 3 cases of the 2X2X2 supercell and the position 4 and 5 cases in the 2X2x1 supercell into consideration, it can be reasoned that the presence of the continuous B-V-B chain would strengthen the expansion of the lattice along the chain direction. Another possible explanation would just be that the high K composition of the supercell would lead to a larger lattice deformation along all directions. But one thing seems to be clear, the B-V-B vectors direction would tend to have a smaller change compared to the other two directions no matter what is the K composition and where is F vacancy position.

3.5 Structure distortion and dipole-dipole configuration analysis of the cell with 12.5% K composition (2x2x4 supercell)

From the previous discussion, it is still not clear whether one or two cell directions are more subject to change when performing geometry optimization than others, and what cell symmetry the optimized cell tends to have. Additionally, it seems that the relative position between the K_{Pb} and V_F can influence both the systems' ground state energy and the symmetry of the optimized cell. By considering the K_{Pb}-V_F pair as a dipole, it is also interesting to study the dipole-dipole interactions within one supercell. Therefore, the 2X2X4 supercell was generated and displayed in Fig 19. In the 2X2X4 supercell, two F vacancies are formed along with the doped two K atoms, corresponding to a K composition equal to 12.5%. An overall number of eight different dipole-dipole combinations are tested here, which can be divided into two sets. The difference between these two sets lies in where the first F vacancy position is relative to the doped K atom, denoted as 1 or 2, and the second F vacancy would have the same four possible positions to sit for both sets. The two dipoles investigated here could be in parallel with each other and connected head to head (1-A), they can also be perpendicular to each other and connected head to head (2-A), and they can also be parallel with each other and connected head to tail (1-B, 2-C), or perpendicular to each other and not connected (1-C, 2-B, 2-D), they can even be parallel with each other and not connected (1-D). The possible positions for the two F vacancies are shown in Fig 19.

Since the material structure experiences a cubic to tetragonal phase transition at a certain K composition, if the reorientation of the dipoles is involved in this process, one can expect that when the two dipoles are connected head to tail along the c direction, the system would be more preferred energetically due to the likelihood of inducing the phase transition. This corresponds to the investigated 1-B case here. As a matter of fact, the 1-B and 2-C positions investigated here are actually equivalent, the same scenario also applies for the 1-C, 2-B, and 2-D positions. This can be further proved by the energy calculation for them as shown in Fig. 20. The equivalent positions exhibit the same ground state energy not surprisingly. From Fig 20, it can be seen that indeed when the two dipoles are connected head to tail with each other, the systems tend to be more stable. The case where the two dipoles are perpendicular to each other and not connected is the second most stable structure. It can be argued from these findings that two vacancies being connected to the same cation would lead to a less stable structure. The 1-D case where two vacancies are parallel to each other and connected to the same Pb atom tested here turns out to be the least energetically favorable combination, which could have something to do with the Pb atom in between the two vacancies. The absolute energy difference per atom between the most and least stable structures tested here has the same magnitude as the values in the 2X2X1 and 2X2X2 supercells, being around 20meV per atom.

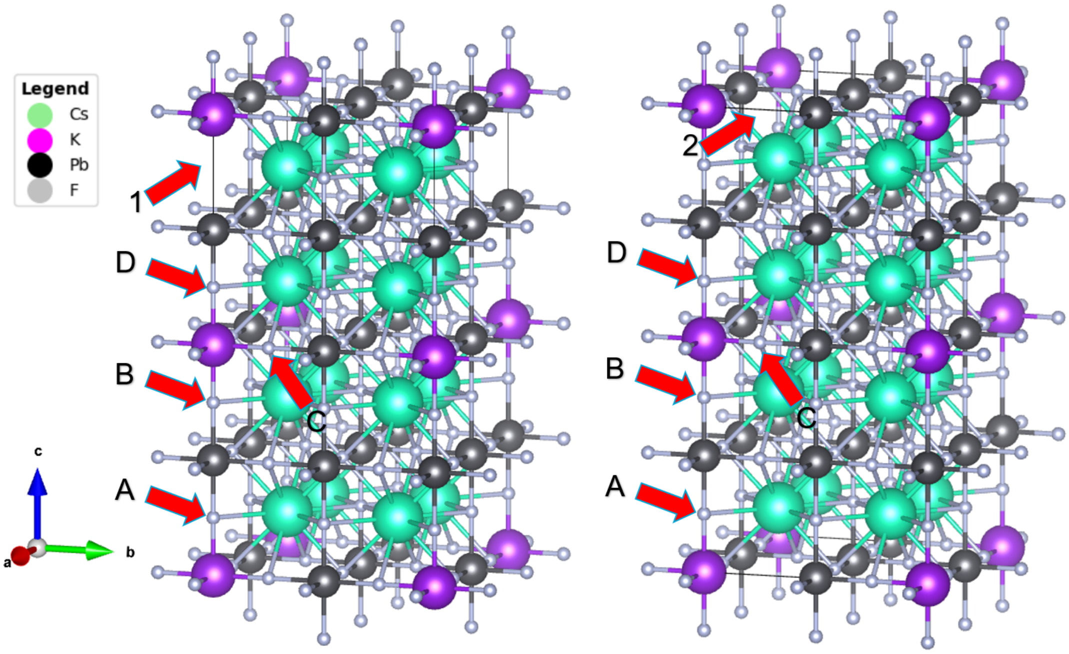

Figure 19: 2X2X4 K doped $CsPbF_3$ supercell with two Pb atoms replaced by two K atoms while generating two F vacancies, corresponding to a K composition equals 12.5%. This graph shows the notation for the different combinations of the two vacancy positions investigated in this project with one K atom located at the origin position. Left: The first F vacancy is located at position 1 and the second vacancy chooses one position from A-D to sit, the notation can be illustrated as 1-A, 1-B, etc. Right: The first F vacancy is located at position 2 and the second vacancy chooses one position from A-D to sit, the notation can be illustrated as 2-A, 2-B, etc. The available positions for F vacancies are indicated with the red arrow. The crystal structure is visualized and retrieved using VESTA(Momma & Izumi, 2008).

By checking the variation of the lattice parameters and cell volumes for all these positions shown in Table 5 and Table 6 respectively, several findings can be presented here. Firstly, all the cases tested here undergo a cell volume shrinkage except the 1-A and 2-A cases, which are not the ones with the lowest ground state energy calculated. The cell volume of case 1-D here changes the most, it is also the least energetically favorable case tested here. Secondly, from the lattice parameter table, one can argue that the optimized cells have at least two components to be the same for up to the second digit after the decimal point. This suggests that the relaxed cells tend to follow a tetragonal structure. But the c/a ratio for these cases is not always less than 1 despite that the cell volume is contracting, this is not exactly consistent with the suggestions in the previous research.(Wang & Ma, 2022) As for the changes in each individual crystal direction, no general trends are found that can be applied to all cases, somethings are even presented counter-intuitively, for instance, the c direction changes in the 1-B and 1-D cases are in the two opposite direction. It would be helpful to carry out further research for analyzing the structure variations observed here. Despite all the remaining questions for future investigation, the study here proved that when the K_{Pb}-V_F dipoles are in parallel with each other and connected head to tail, the resulting configuration is more energetically favorable. Furthermore, this configuration would also likely trigger the cubic to tetragonal phase transition, which matches well with the experimental observation.(Wang & Ma, 2022)

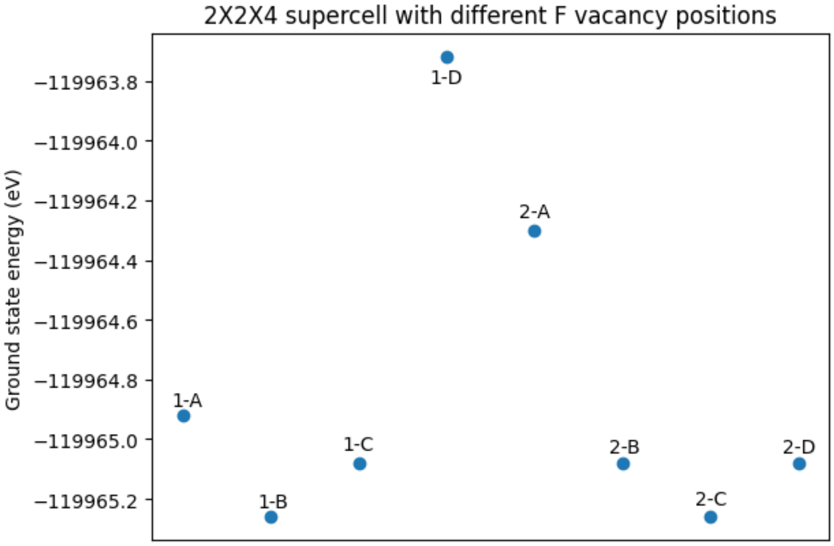

Figure 20: Ground state energy of the 2X2X4 supercell with respect to the different positions for the two F vacancies in one supercell.

Table 5: The lattice parameter change of the 2X2X4 supercell after geometry optimization for the two F vacancies at different positions. The lattice parameter is normalized and displayed as one cubic unit cell.

First F vacancy position	Second F vacancy position	Original lattice parameter of the cubic unit cell (Å)	Optimized lattice parameter of one unit cell (ÅXÅXÅ)
1	A	4.90	4.92X4.92X4.87
	B	4.90	4.91X4.91X4.88
	C	4.90	4.90X4.90X4.91
	D	4.90	4.89X4.89X4.92
2	A	4.90	4.91X4.91X4.91
	B	4.90	4.90X4.90X4.90
	C	4.90	4.90X4.92X4.90
	D	4.90	4.90X4.90X4.91

Table 6: The cell volume change of the 2X2X4 supercell after geometry optimization for the two F vacancies at different positions.

First F vacancy position	Second F vacancy position	Original cell volume (Å^3)	Optimized cell volume (Å^3)	Volume expansion (Å^3)	Volume expansion rate (%)
1	A	1886.65	1887.18	0.53	0.03
	B	1886.65	1883.87	-2.78	-0.15
	C	1886.65	1882.67	-3.97	-0.21
	D	1886.65	1879.49	-7.16	-0.38
2	A	1886.65	1889.52	2.88	0.15
	B	1886.65	1882.63	-4.02	-0.21
	C	1886.65	1884.84	-1.81	-0.10
	D	1886.65	1882.93	-3.71	-0.20

3.6 Nudged Elastic Band calculation

Nudged elastic band (NEB) calculation is a way to search for the saddle points and investigate the energy landscape between two known configurations. It first generates a set of images with equal spacing to each other in between the initial and final endpoints. Then the NEB calculation would optimize the energy for each image by nudging them to counteract the elastic forces. The image with the highest energy is considered to be the transition state in between. NEB calculation can be very helpful in finding the possible reaction mechanisms and pathways for applications like the diffusion of ions.(Henkelman, Uberuaga, & Jónsson, 2000)

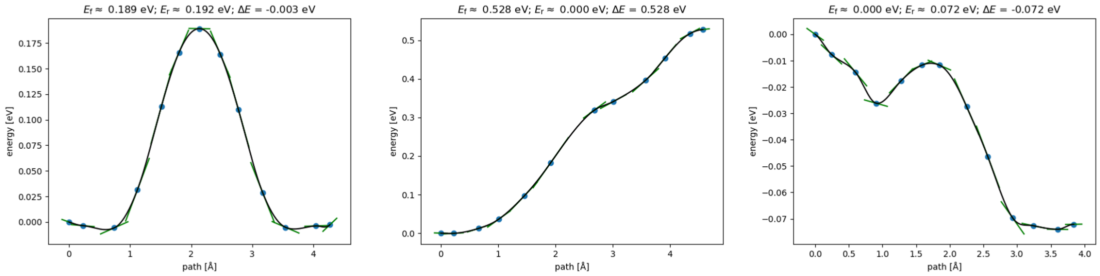

Figure 21: NEB calculation results for the F vacancy in the 2X2X2 supercell moving from position 1 to another position 1 (Left), from position 1 to position 2 (Middle), from position 2 to position 3 (Right). The y-axis represents the ground state energy, and the x-axis indicates the distance of what the F vacancy has moved. E_f, E_r, and ΔE represent the energy barrier height, the normalized energy of the initial state, and the $E_{final} - E_{initial}$, respectively.

In this thesis work, NEB calculations are used to study the energy landscapes of the vacancy movement, focusing on the three possible positions in the 2X2X2 K doped $CsPbF_3$ supercell, aka PK12.5. Three calculations are carried out, namely, the vacancy moving from position 1 to another position 1 connecting to the same K atom, noted as 1-1, from position 1 to position 2 connecting to the same Pb atom, noted as 1-2, and from position 2 to position 3 connecting to the same Pb atom, noted as 2-3. The animations of the vacancy movements of these three experiments can be visualized using the link provided in the appendix. Fig 21 shows the generated results from these three calculations.

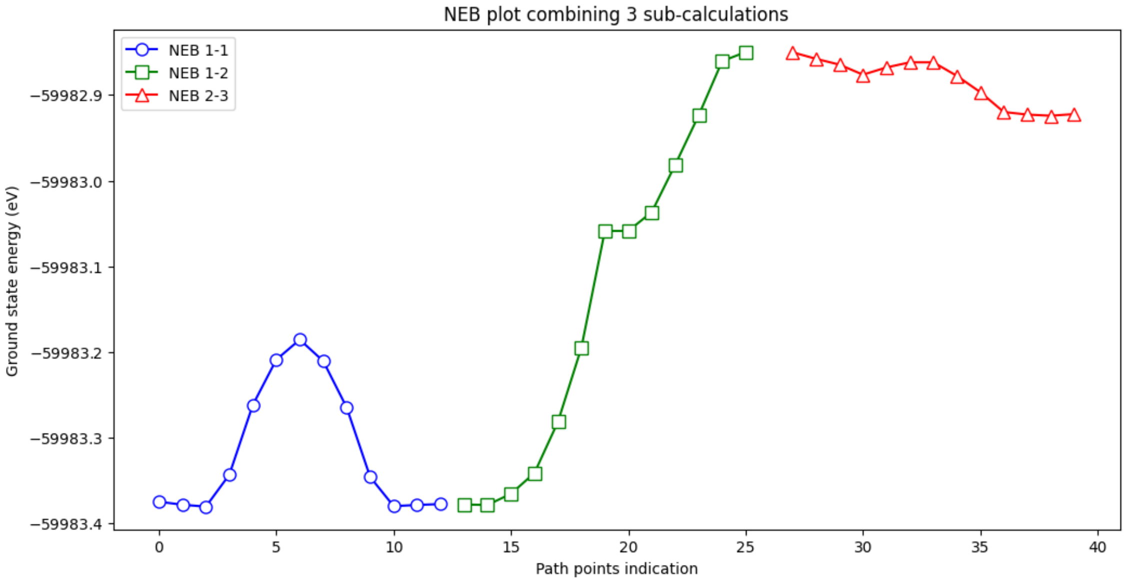

Figure 22: NEB plot combining 3 sub-calculations, the F vacancy here moves from one position 1 to another position 1, then to a position 2 and to a position 3 in the end. The x-axis here serves as an illustration of the path point sequence from the previous 3 sub-plots. The y-axis here indicates the ground state energy.

The NEB 1-1 calculation exhibits an energy barrier for F vacancy to move from one position 1 to another position 1 to be 0.189eV, corresponding to around 4.85meV per atom which is relatively low. The results here suggest that F vacancy in this supercell can easily move from one position 1 to another position 1 that is connected to the same K atom. The initial and final state does not appear to be the local minima on the energy landscape, especially for the initial state, meanwhile, the initial and final state do not have exactly the same energy as expected. One may argue that the 0.003eV would be the numerical accuracy here, thus also explaining those points that appeared with slightly lower energy than the two endpoints. The NEB 1-2 case does not show a clear energy barrier, a possible reason could be that the initial guess of the vacancy movement trajectory or the intermediate state is not very accurate. If taking the calculated 0.528eV here into account, this would correspond to around 14meV per atom, which is still quite low. The NEB 2-3 calculation result demonstrates that position 2 is less favorable energetically than position 3, which does not agree with the results shown in Fig 14, even though the energy difference is quite small. Additionally, the initial state here is clearly not the local minimum. The abnormalities observed here still remain to be open questions.

Next, these three different NEB plots are compared to appreciate the different scales and overall energy landscape. As can be seen from Fig 22, based on the data obtained here, it is easier for the F vacancy to move between two positions 1 or between position 2 and position 3, compared to moving from position 1 to position 2. To rationalize this finding, it is also helpful to consider the coulombic interactions and the K_{Pb}-V_F dipoles. For the NEB 1-1 or 2-3 case, the F vacancy in the initial and final structures are connected to the same K or Pb atom. Its movement would be similar to a bond rotation process, with no other significant constraints, this case would have a relatively low energy barrier. Also considering that the V_F is attracted by the K_{Pb} in case NEB 1-1 while repelled by the Pb atom in case NEB 2-3, the barrier for 1-1 case would be higher than 2-3 case. As for the NEB 1-2 case, despite that the F vacancy is still moving in between different positions that are connected with the same Pb atom, the F vacancy in the initial configuration is also connected to a K_{Pb}, while just in between two Pb atoms for the end configuration. In order to make this happen, the K_{Pb}-V_F dipole in the initial configuration would first need to be broken, which would result in a much higher energy barrier for the F vacancy to move compared to the other two cases examined here. Overall, the K_{Pb} would have a tendency to keep the V_F thus making the V_F less mobile, and one could speculate that if the K composition is too high, then there will not be enough mobile V_F available to display a high ionic conductivity. In the previously mentioned literature(Wang et al., 2022), the K-doped $CsPbF_3$ material with the maximum ionic conductivity observed has a K composition equal to 10%, where they suggested that this is caused by a trade-off between the number of V_F and the decreasing lattice parameter that leads to less space for the V_F to move. If the hypothesis introduced in this project holds true, then this maximum conductivity point observed experimentally could also be explained as the trade-off between the number of total V_F and the V_F that are "fixed" to the K_{Pb}.

At this point, it comes to mind that moving the F vacancy directly from position 1 to position 3 would be a case worth investigating. This could be used to test the above-mentioned hypothesis, and to grep a comprehensive understanding of all the possible cases that could happen for the F vacancy movement in the 2X2X2 supercell. Therefore, the scenario where the F vacancy moves from position 1 to position 3 is also tested and shown in Fig 23, the animation can also be checked in the appendix.

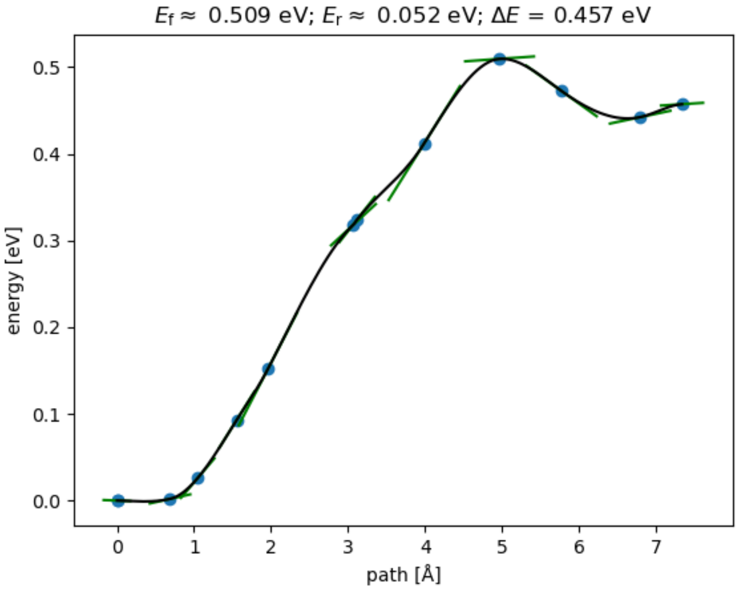

Figure 23: NEB calculation results with F vacancy moving from position 1 to position 3. The y-axis represents the ground state energy, and the x-axis indicates the distance of what the F vacancy has moved. E_f, E_r, and ΔE represent the energy barrier height, the normalized energy of the initial state, and the $E_{final} - E_{initial}$, respectively.

It needs to be pointed out that Fig 23 here does not contain the vacancy moving from one position 1 to another position 1 case compared to Fig 22. Here, the F vacancy first breaks the K_{Pb}-V_F interaction and moves to a Pb atom neighboring the connected Pb atom initially. The plot displayed here is closer to the results one would expect with a high energy barrier close to the case NEB 1-2, despite that the final state is still not exactly the local minimum on the energy landscape. Additionally, this energy barrier and the barriers in all cases tested here could also be potentially induced by the Cs atoms in the crystal structure, with their large size and effective positive charge the same as the vacancy. This factor could at least provide part of the contribution to the F vacancy diffusion barriers. Nevertheless, the energy barrier calculated here is 509meV, corresponding to 13meV per atom, which is only about half of the 25meV per atom corresponding to the room temperature. This small number could indicate the relative easiness for F vacancy to diffuse in the K-doped $CsPbF_3$ material system with a composition equal to 12.5%. Thereby offering an insight to rationalize the high ionic conductivity observed experimentally for this promising material.

It is noted that some inconsistency is presented between the energy value calculated here and the energy obtained from previously performed geometry optimization. Further pilot calculations performed revealed that this is most likely to be attributed to the different electronic energy tolerances used, with the geometry optimization using a number 1e-6 and the NEB calculation having 1e-5 to reduce the computational resources needed. Hence, the energy value from the NEB calculations and geometry optimizations are not directly related, they should be analyzed separately in this case. But still, the trends should be comparable. If time and computational power allow, all calculations performed with the same parameters would definitely be ideal for further study.

To summarize the NEB calculations, based on the results presented here, first of all, it is found that if the diffusion of F vacancy would require the breaking of K_{Pb}-V_F dipoles, then a large energy barrier needs to be overcome. Otherwise, the energy barrier would be lower. Secondly, if the F vacancy is moving around the same Pb atom, the energy barrier would be lower than the case where the F vacancy moves around the same K atom, which could be attributed to the different coulombic interactions between K_{Pb}-V_F and Pb-V_F. Moreover, the decreasing ionic conductivity observed experimentally upon the K composition reaching a certain level can potentially be explained by the K_{Pb} trying to keep V_F fixed thus resulting in decreased ionic mobilities of the charge carriers. Last but not least, some unexpected results are also generated from the NEB calculations. To explain these abnormalities and to further prove the previously mentioned hypothesis, further investigation is required.

4 Conclusions

With climate change becoming more and more tangible and perceptible, actions are required to be taken fast. Going through an energy transition to replace the current fossil fuel-based energy system with a renewable energy-based one is the linchpin of dealing with climate change. For an energy system fully powered by renewable sources, a proper and efficient energy storage method is essential. Solid-state batteries are considered to be a promising next-generation technology for energy storage applications, where finding a well-performing solid-state ionic conductor is the key. Countless research and efforts have been focused on this important and challenging field including this project.

This thesis work investigated a promising type of fluoride ion conductor, the K-doped $CsPbF_3$ material, which could be potentially used as the solid-state electrolyte for future solid-state fluoride ion batteries. Density functional theory is applied here to study this material focusing on calculating its NMR parameters. A thorough analysis of this material using the obtained results is presented, from the structure exploration of the pure $CsPbF_3$ and the K-doped $CsPbF_3$ supercells to the vacancy diffusion energy landscape in the crystal structure, as well as the interpretation of the calculated NMR parameters. Despite the presence of a few open-ended questions and some not fully understood results, several findings can be concluded here.

Firstly, this study further proved that for the pure $CsPbF_3$ structure, it favors a rhombohedral configuration at 0K. A lattice expansion caused by the increased temperatures could be one of the driving forces for its rhombohedral to cubic phase transition happening at 187K. At temperatures above 187K, this material tends to follow a cubic structure instead of a tetragonal structure from the energy perspective.

Secondly, from the ^{19}F NMR calculation of the tetragonal $CsPbF_3$ structures, it is found that simply measuring the Cs-F distance, Pb-F distance or the cell volume alone is not enough to explain the variation trend of the calculated ^{19}F isotropic chemical shielding data. Evaluating how the structural changes would influence the σ_{iso} value requires taking the whole system into consideration instead of just focusing on some neighboring atoms of the F atom. This finding is further proved by the NMR calculation for the K-doped $CsPbF_3$ systems.

Thirdly, the coulombic interaction can be applied to explain the forces felt by all the atoms(ions) upon doping K into the $CsPbF_3$ system. These forces are the reason that leads to the new crystal structure for the fully relaxed cell. Under this circumstance, the F vacancy would act as an effective cation and the doped K would act as an effective anion. The results suggest that both the direction and the scale of the forces can be rationalized with the coulombic interaction.

Next, for both the 2X2X1 and 2X2X2 supercells investigated here, which correspond to a K composition being 25% and 12.5% respectively, the most energetically favorable configuration in both cases have the F vacancy to be right next to the doped K. Generally speaking, the ground state energy value and the cell volume variation rate for the optimized cells get larger with the increasing K-F distance. As for the case where two vacancies are present together in the supercell, which is the 2X2X4 supercell tested here in this project, the K_{Pb}-V_F dipoles can be used for analysis. It turns out that when the two dipoles are in parallel with each other and connected head to tail, the structure has the lowest ground state energy, and this dipole configuration is also among all the tested cases the one that could most likely lead to the cubic to tetragonal phase transition. Predominantly, when the distance between two vacancies gets larger, the structure will be more energetically favorable. Moreover, with two vacancies coexisting in the supercell and corresponding to a K composition being 12.5%, the cell volume of the crystal structure most likely will decrease, considering that the cells have a tendency to go through a cubic to tetragonal phase transition as well, the results presented in this study is in line with what has been found previously(Wang & Ma, 2022).

Last but not least, this project performed several NEB calculations to probe into the vacancy diffusion energy landscape. In the 2X2X2 supercell with 12.5% K composition, the results suggest that the energy barrier for the vacancy to diffuse between positions is relatively low, even less than 15meV per atom. Compared with the energy per atom being 25meV at room temperature, this finding could serve as a reason to explain the high ionic conductivity observed for this material in general. This study also finds that the K_{Pb} in the crystal structure can demobilize its neighboring F vacancies, which would decrease the ionic conductivity of this material when the K composition reaches a certain level. These results generated from the NEB calculations here can be employed to rationalize the trends observed experimentally in the previous research.(Wang et al., 2022)

5 Recommendations and Outlooks

Until this point, it goes without further emphasizing the significance of solid-state batteries in terms of energy transition. The K-doped $CsPbF_3$ shows very promising potential that could lead to the appearance of the next generation fluoride ion solid-state batteries. A clear understanding of its structure and property correlations is of vital importance, which is exactly the focus of this thesis project. Due to the limited time and computational resources available for this project, some problems raised from the results still remain unsolved, and some interesting directions are also worth further investigation. Along with the perceptions resulting from the preceding of this project, they will be presented here to serve as a reference for future studies.

First and foremost, a more thorough understanding of the theories behind is definitely going to be more helpful for studying this topic in general. For example, a deeper understanding of the principles of NMR could facilitate a clearer and more detailed interpretation of the NMR parameters calculated here, which could then help to draw a better picture of this material's local structure, thus understanding better its good properties presented and the possible enhancement direction.

Secondly, the Pb lone pair in the $CsPbF_3$ material is something that deserves further investigation. Several open questions still remain here. For example, how does the presence of this lone pair influence the polarization of this material? How to visualize the lone pair in the material's charge density plot or how to explain the uniform charge density observed around Pb atoms in the charge density plot presented previously? How does the Pb lone pair influence the structural deformation of the K-doped $CsPbF_3$ and how does it facilitate or hinder the movement of F vacancies in the crystal structure?

Thirdly, more complex supercells with different sizes and K compositions could be built and studied. This could help to build a clearer understanding of the phase transitions and other structural changes that happened in the material system with respect to the K composition. By looking into some larger supercells with multiple F vacancies and multiple combination possibilities for these F vacancies, the examined case could be a better approximation of the material system in reality and therefore obtain more convincing results.

Next, the NEB calculations carried out in this thesis are still quite preliminary. Similar to the previous point, further analysis could be carried out with different K compositions and more F vacancies in the supercell thus offering more possible diffusion paths. Questions still remain to be explored here including, why the 1-2 case does not contain a clear energy barrier? Why the 2-3 case here is inconsistent with the previous energy calculation? Since the NEB calculations are dependent on the initial guess of the path, this could result in some systematic errors. To deal with it, DFT-D could be potentially helpful here to increase the accuracy when calculating the potential energy surface. Molecular dynamics (MD) could also be exploited prior to the NEB calculations in order to have a rough idea of the vacancy movement trajectory beforehand.

Last but not least, some additional studies could also be further carried on as a complement to this work to obtain an even more thorough understanding of the K-doped $CsPbF_3$ material. For example, since all the studies looked into here are based on the 0K temperature, ab initio MD could be used as the next stage to study this material at the operating temperature when assembled into batteries. Calculations or experiments could also be specifically designed to study why this material also possesses a wide electrochemical stability window, and to find out what would be the material structure that contributes to this. Along with all the above-mentioned angles for future investigation, this could provide a more convincing insight regarding the detailed structure information of the K-doped $CsPbF_3$ material, and the possibility of tuning this material for better performance and eventually, large-scale application.

References

Ashbrook, S. E., & Dawson, D. M. (2013). Exploiting periodic first-principles calculations in nmr spectroscopy of disordered solids. *Accounts of Chemical Research*, *46*(9), 1964–1974.

Bhumla, P., Gill, D., Sheoran, S., & Bhattacharya, S. (2021). Origin of rashba spin splitting and strain tunability in ferroelectric bulk cspbf3. *The Journal of Physical Chemistry Letters*, *12*(39), 9539–9546.

Boltalin, A., Korenev, Y. M., & Sipachev, V. (2007). A theoretical study of the structure and thermochemical properties of alkali metal fluoroplumbates mpbf3. *The Journal of Physical Chemistry A*, *111*(28), 6534–6538.

Boltalin, A., Rykov, A., & Korenev, Y. M. (1990). Determination of dissociation enthalpies of kpbf 3, rbpbf 3, cspbf 3 complex molecules. *Zhurnal Neorganicheskoj Khimii*, *35*(11), 2908–2911.

Bonhomme, C., Gervais, C., Babonneau, F., Coelho, C., Pourpoint, F., Azais, T., ... others (2012). First-principles calculation of nmr parameters using the gauge including projector augmented wave method: a chemist's point of view. *Chemical Reviews*, *112*(11), 5733–5779.

CASTEP Documentation. (2023). *Castep neb tutorial.* Retrieved from https://castep-docs.github.io/castep-docs/tutorials/NEB/neb_tutorial/

CASTEP keywords. (2023). https://www.tcm.phy.cam.ac.uk/castep/documentation/WebHelp/content/modules/castep/expcastepkeywords.htm?tocpath=CASTEP%20keywords%7C_____0.

Charpentier, T. (2011). The paw/gipaw approach for computing nmr parameters: A new dimension added to nmr study of solids. *Solid state nuclear magnetic resonance*, *40*(1), 1–20.

China Meteorological Administration. (2023). *China meteorological administration august 2023 press conference.* Retrieved from https://www.cma.gov.cn/wmhd/2011wzbft/2011wzxzb/xwfbh_2308/index.html

Clark, S. J., Segall, M. D., Pickard, C. J., Hasnip, P. J., Probert, M. I., Refson, K., & Payne, M. C. (2005). First principles methods using castep. *Zeitschrift für kristallographie-crystalline materials*, *220*(5-6), 567–570.

Delft High Performance Computing Centre (DHPC). (2022). *DelftBlue Supercomputer (Phase 1).* https://www.tudelft.nl/dhpc/ark:/44463/DelftBluePhase1.

Dudney, N. J., West, W. C., & Nanda, J. (2015). *Handbook of solid state batteries* (Vol. 6). World Scientific.

Duer, M. J. (2008). *Solid state nmr spectroscopy: principles and applications.* John Wiley & Sons.

Engel, E., & Dreizler, R. M. (2011). Density functional theory. *Theoretical and mathematical physics*, 11–56.

Famprikis, T., Canepa, P., Dawson, J. A., Islam, M. S., & Masquelier, C. (2019). Fundamentals of inorganic solid-state electrolytes for batteries. *Nature materials*, *18*(12), 1278–1291.

Franchini, C., Reticcioli, M., Setvin, M., & Diebold, U. (2021). Polarons in materials. *Nature Reviews Materials*, *6*(7), 560–586.

Goodenough, J. B. (1984). Review lecture-fast ionic conduction in solid. *Proceedings of the Royal Society of London. A. Mathematical and Physical Sciences*, *393*(1805), 215–234.

Griffin, J. M., Yates, J. R., Berry, A. J., Wimperis, S., & Ashbrook, S. E. (2010). High-resolution 19f mas nmr spectroscopy: structural disorder and unusual j couplings in a fluorinated hydroxy-silicate. *Journal of the American Chemical Society*, *132*(44), 15651–15660.

Groszewicz, P. B. (2021). Nmr spectroscopy of electroceramics–applications to lead-free perovskite oxides. *Open Ceramics*, *5*, 100083.

Henkelman, G., Uberuaga, B. P., & Jónsson, H. (2000). A climbing image nudged elastic band method for finding saddle points and minimum energy paths. *The Journal of chemical physics*, *113*(22), 9901–9904.

Hore, P. J. (2015). *Nuclear magnetic resonance*. Oxford University Press, USA.

Jain, A., Ong, S. P., Hautier, G., Chen, W., Richards, W. D., Dacek, S., . . . others (2013). Commentary: The materials project: A materials genome approach to accelerating materials innovation. *APL materials*, *1*(1).

Janek, J., & Zeier, W. G. (2016). A solid future for battery development. *Nature energy*, *1*(9), 1–4.

Janek, J., & Zeier, W. G. (2023). Challenges in speeding up solid-state battery development. *Nature Energy*, *8*(3), 230–240.

Jmol development team. (2023). *Jmol: an open-source java viewer for chemical structures in 3d.* Retrieved from `http://www.jmol.org/`

Kamitsos, E. I., Karakassides, M., & Chryssikos, G. D. (1986). A vibrational study of lithium sulfate based fast ionic conducting borate glasses. *The journal of physical chemistry*, *90*(19), 4528–4533.

Koohi-Fayegh, S., & Rosen, M. A. (2020). A review of energy storage types, applications and recent developments. *Journal of Energy Storage*, *27*, 101047.

Kraft, M. A., Culver, S. P., Calderon, M., Bo¨cher, F., Krauskopf, T., Senyshyn, A., . . . Zeier, W. G. (2017). Influence of lattice polarizability on the ionic conductivity in the lithium superionic argyrodites li6ps5x (x= cl, br, i). *Journal of the American Chemical Society*, *139*(31), 10909–10918.

Li, C., Wang, Z.-y., He, Z.-j., Li, Y.-j., Mao, J., Dai, K.-h., . . . Zheng, J.-c. (2021). An advance review of solid-state battery: Challenges, progress and prospects. *Sustainable Materials and Technologies*, *29*, e00297.

Li, L., Qian, Y., Leng, X., Cui, X., Duan, H., Lee, M.-H., . . . Jing, Q. (2022). First-principles investigation about different sequence of stereochemical activity and birefringence in antimony halides. *physica status solidi (b)*, *259*(7), 2100576.

Li, Z., Yang, M., Park, J.-S., Wei, S.-H., Berry, J. J., & Zhu, K. (2016). Stabilizing perovskite structures by tuning tolerance factor: formation of formamidinium and cesium lead iodide solid-state alloys. *Chemistry of Materials*, *28*(1), 284–292.

Ma, C.-G., & Brik, M. (2012). Hybrid density-functional calculations of structural, elastic and electronic properties for a series of cubic perovskites csmf3 (m= ca, cd, hg, and pb). *Computational materials science*, *58*, 101–112.

Maddox, J. (1988). Crystals from first principles. *Nature*, *335*, 201–201.

Materials project. (2023). `https://next-gen.materialsproject.org/materials/mp-20282?formula=CsPbF3`.

Mattsson, A. E., Armiento, R., Schultz, P. A., & Mattsson, T. R. (2006, May). Nonequivalence of the generalized gradient approximations pbe and pw91. *Phys. Rev. B*, *73*, 195123. Retrieved from `https://link.aps.org/doi/10.1103/PhysRevB.73.195123` doi: 10.1103/PhysRevB.73.195123

Megaw, H. D. (1946). Crystal structure of double oxides of the perovskite type. *Proceedings of the Physical Society*, *58*(2), 133.

Momma, K., & Izumi, F. (2008). Vesta: a three-dimensional visualization system for electronic and structural analysis. *Journal of Applied crystallography*, *41*(3), 653–658.

Morgan, B. J. (2021). *Understanding fast-ion conduction in solid electrolytes* (Vol. 379) (No. 2211). The Royal Society.

Murtaza, G., Ahmad, I., Maqbool, M., Aliabad, H. R., & Afaq, A. (2011). Structural and optoelectronic properties of cubic cspbf3 for novel applications. *Chinese Physics Letters*, *28*(11), 117803.

Muy, S., Schlem, R., Shao-Horn, Y., & Zeier, W. G. (2021). Phonon–ion interactions: Designing ion mobility based on lattice dynamics. *Advanced Energy Materials*, *11*(15), 2002787.

NASA Earth Observatory. (2023). *Relentless wildfires in canada.* Retrieved from https://earthobservatory.nasa.gov/images/151696/relentless-wildfires-in-canada

Panchmatia, P. M., Orera, A., Rees, G. J., Smith, M. E., Hanna, J. V., Slater, P. R., & Islam, M. S. (2011). Oxygen defects and novel transport mechanisms in apatite ionic conductors: combined 17o nmr and modeling studies. *Angewandte Chemie International Edition*, *50*(40), 9328–9333.

Pasta, M., Armstrong, D., Brown, Z. L., Bu, J., Castell, M. R., Chen, P., ... others (2020). 2020 roadmap on solid-state batteries. *Journal of Physics: Energy*, *2*(3), 032008.

Qian, J., Xu, B., & Tian, W. (2016). A comprehensive theoretical study of halide perovskites abx3. *Organic Electronics*, *37*, 61–73.

Reuters. (2023). *What caused record rainfall in beijing, northern china.* Retrieved from https://www.reuters.com/world/china/what-caused-record-rainfall-beijing-northern-china-2023-08-02/

Roma, G., Marronnier, A., & Even, J. (2020). From latent ferroelectricity to hyperferroelectricity in alkali lead halide perovskites. *Physical Review Materials*, *4*(9), 092402.

Rutter, M. J. (2018). C2x: A tool for visualisation and input preparation for castep and other electronic structure codes. *Computer Physics Communications*, *225*, 174–179.

Sadoc, A., Body, M., Legein, C., Biswal, M., Fayon, F., Rocquefelte, X., & Boucher, F. (2011). Nmr parameters in alkali, alkaline earth and rare earth fluorides from first principle calculations. *Physical Chemistry Chemical Physics*, *13*(41), 18539–18550.

Sears, R., Guo, Q. Z., & Mackey, H. (1984). Electron-coupled nuclear spin–spin interactions in cubic pbf2 and the 19f chemical shift. *The Journal of chemical physics*, *80*(11), 5448–5452.

Segall, M., Lindan, P. J., Probert, M. a., Pickard, C. J., Hasnip, P. J., Clark, S., & Payne, M. (2002). First-principles simulation: ideas, illustrations and the castep code. *Journal of physics: condensed matter*, *14*(11), 2717.

Shannon, R. D. (1976). Revised effective ionic radii and systematic studies of interatomic distances in halides and chalcogenides. *Acta crystallographica section A: crystal physics, diffraction, theoretical and general crystallography*, *32*(5), 751–767.

Sholl, D. S., & Steckel, J. A. (2022). *Density functional theory: a practical introduction.* John Wiley & Sons.

Smith, E. H., Benedek, N. A., & Fennie, C. J. (2015). Interplay of octahedral rotations and lone pair ferroelectricity in cspbf3. *Inorganic Chemistry*, *54*(17), 8536–8543.

Sturniolo, S., Green, T. F., Hanson, R. M., Zilka, M., Refson, K., Hodgkinson, P., ... Yates, J. R. (2016). Visualization and processing of computed solid-state nmr parameters: Magresview and magrespython. *Solid state nuclear magnetic resonance*, *78*, 64–70.

Sturniolo, S., Hasnip, P., Byrne, P., Hodgkinson, P., Probert, M., & Kermode, J. (2022). Support for advanced transition state search techniques in castep.

Szczuka, C., Karasulu, B., Groh, M. F., Sayed, F. N., Sherman, T. J., Bocarsly, J. D., . . . others (2022). Forced disorder in the solid solution li3p–li2s: A new class of fully reduced solid electrolytes for lithium metal anodes. *Journal of the American Chemical Society*, *144*(36), 16350–16365.

Tuller, H. L., & Moon, P. K. (1988). Fast ion conductors: future trends. *Materials Science and Engineering: B*, *1*(2), 171–191.

Walsh, A., & Watson, G. W. (2005). The origin of the stereochemically active pb (ii) lone pair: Dft calculations on pbo and pbs. *Journal of Solid State Chemistry*, *178*(5), 1422–1428.

Wang, J., Hao, J., Duan, C., Wang, X., Wang, K., & Ma, C. (2022). A fluoride-ion-conducting solid electrolyte with both high conductivity and excellent electrochemical stability. *Small*, *18*(5), 2104508.

Wang, J., & Ma, C. (2022). Superior room-temperature cycling stability of fluoride-ion batteries enabled by solid electrolytes synthesized by the solid-state reaction. *Science China Materials*, *65*(11), 3025–3032.

Wood, B. C., Varley, J. B., Kweon, K. E., Shea, P., Hall, A. T., Grieder, A., . . . others (2021). Paradigms of frustration in superionic solid electrolytes. *Philosophical Transactions of the Royal Society A*, *379*(2211), 20190467.

World Meteorological Organization. (2023). *Copernicus confirms july 2023 was hottest month ever recorded.* Retrieved from `https://public.wmo.int/en/media/news/copernicus-confirms-july-2023-was-hottest-month-ever-recorded`

Yan, X., Zhang, K., Guo, C., Lu, Y., Du, K., Peng, C., . . . others (2023). Growth and characterization of all-inorganic halide perovskite cspbf3 single crystals. *Crystals*, *13*(5), 765.

A Appendix

A.1 Additional ^{19}F NMR investigation

The NMR isotropic chemical shielding data of a set of F-containing materials was calculated, and using the experimental chemical shift data found in literature,(Sears, Guo, & Mackey, 1984)(Griffin, Yates, Berry, Wimperis, & Ashbrook, 2010)(Sadoc et al., 2011), the shielding versus shift plot was made, parameters used for the calculations can be found in Table 7. To test the influence of different exchange-correlation functionals on the accuracy of the results, two sets of calculations were performed and compared using PBE and R2SCAN exchange-correlation functionals, shown in Fig 24. No significant differences were observed from this comparison, as a result, all the calculations performed in this work used PBE solely.

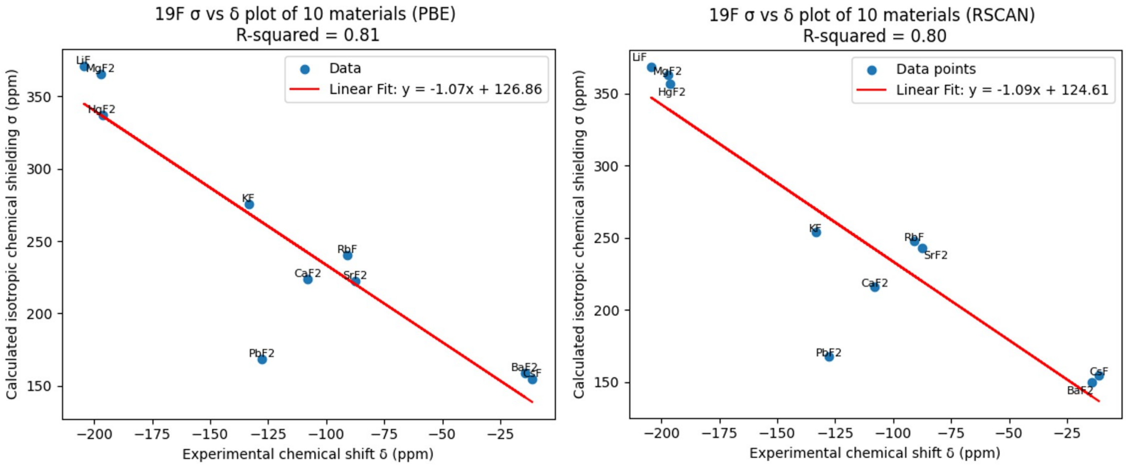

Figure 24: Isotropic chemical shielding versus chemical shift data for ten F-containing materials. Left: calculations and fitting using PBE exchange-correlation functional. Right: calculations and fitting using R2SCAN exchange-correlation functional.

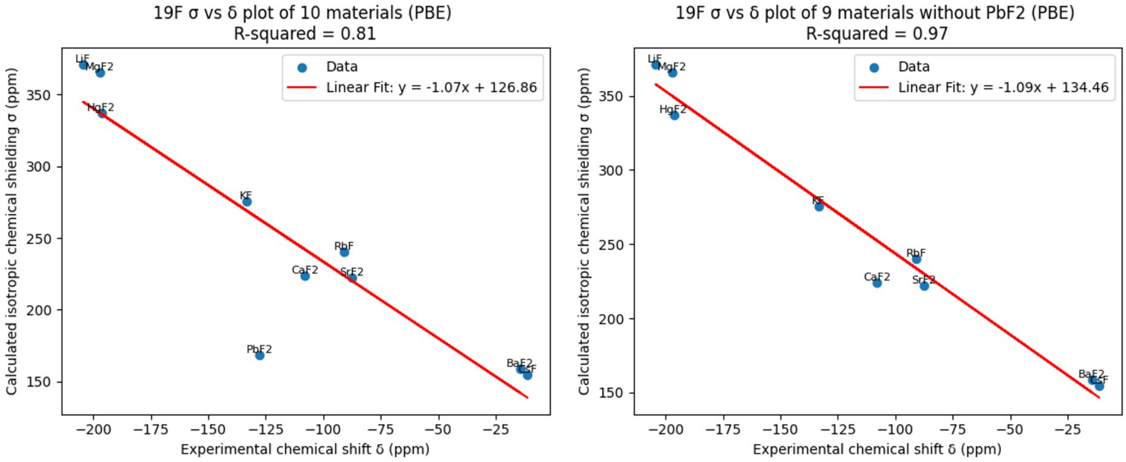

Figure 25: Isotropic chemical shielding versus chemical shift data for F-containing materials. Left: calculations and fitting for ten materials. Right: calculations and fitting excluding PbF_2.

From the calculations and fitting, PbF_2 seems to be an outlier, hence, another fitting excluding PbF_2 was performed, as can be seen from Fig 25. The fitting equation from here can be used to predict the theoretical ^{19}F chemical shift data from the calculated isotropic chemical shielding data of any F-containing materials, and then it can be used to compare with the actual data from experiments. This is not covered by this thesis work. Whether PbF_2, in this case, is truly an outlier still needs some further proof by taking the accuracy of the calculations here into account. Nevertheless, the Pb containing PbF_2 showed something unique here from other materials, which can probably be linked to the presence of the Pb lone pair.

Table 7: Parameters used for the calculations of the σ_{iso} data in the shielding versus shift plots

Materials	k Points Mesh	Energy Cutoff (eV)
CsF	4x4x4	650
PbF2	6x6x6	700
KF	4x4x4	650
CaF2	7x7x7	720
MgF2	6x6x9	720
BaF2	6x6x6	690
LiF	6x6x6	620
HgF2	11x11x11	720
RbF	3x3x3	800
SrF2	3x3x3	800

A.2 Supercell NMR calculation

A.2.1 2X2X1 supercell

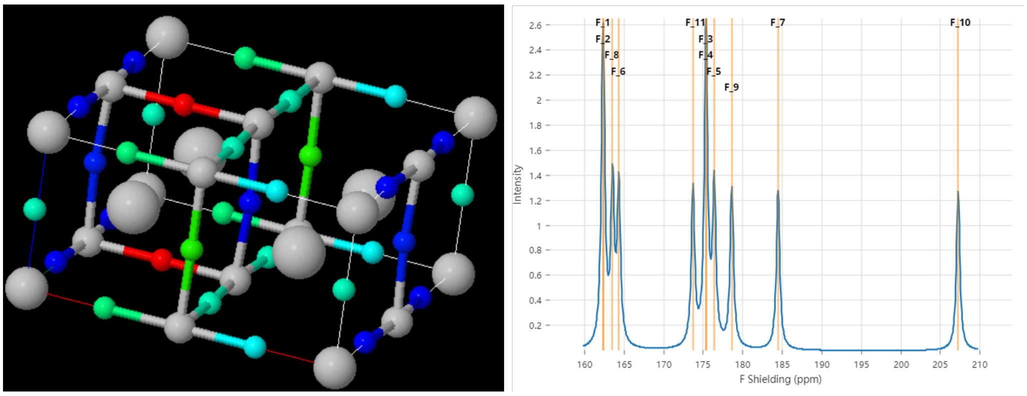

Figure 26: Visualization of the calculated isotropic chemical shielding data for the 2X2X1 supercell with F vacancy located at position 3. Left: the σ_{iso} for each individual F atom displayed in a color scale, with red being the one with the highest value and dark blue being the one with the lowest. Right: the σ_{iso} data for all F atoms showed in the spectrum form. Visualized using MagresView(Sturniolo et al., 2016)

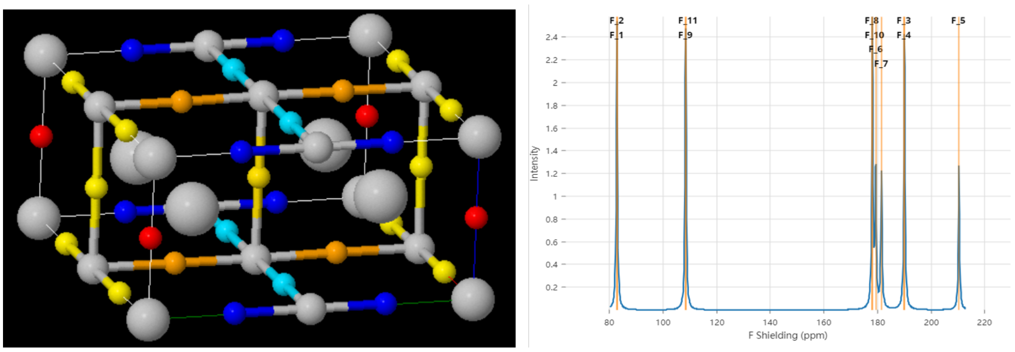

Figure 27: Visualization of the calculated isotropic chemical shielding data for the 2X2X1 supercell with F vacancy located at position 4. Left: the σ_{iso} for each individual F atom displayed in a color scale, with red being the one with the highest value and dark blue being the one with the lowest. Right: the σ_{iso} data for all F atoms showed in the spectrum form. Visualized using MagresView(Sturniolo et al., 2016)

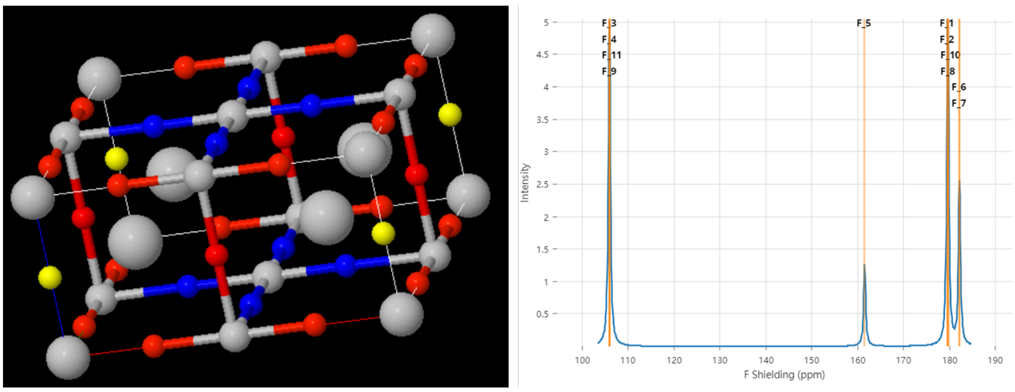

Figure 28: Visualization of the calculated isotropic chemical shielding data for the 2X2X1 supercell with F vacancy located at position 5. Left: the σ_{iso} for each individual F atom displayed in a color scale, with red being the one with the highest value and dark blue being the one with the lowest. Right: the σ_{iso} data for all F atoms showed in the spectrum form. Visualized using MagresView(Sturniolo et al., 2016)

A.2.2 2X2X2 supercell

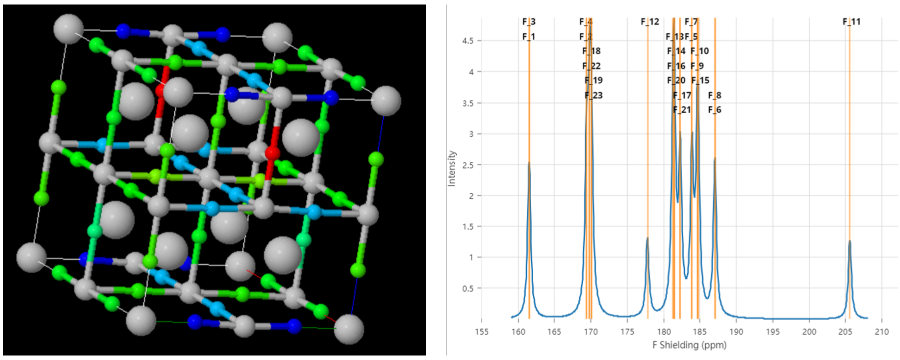

Figure 29: Visualization of the calculated isotropic chemical shielding data for the 2X2X2 supercell with F vacancy located at position 2. Left: the σ_{iso} for each individual F atom displayed in a color scale, with red being the one with the highest value and dark blue being the one with the lowest. Right: the σ_{iso} data for all F atoms showed in the spectrum form. Visualized using MagresView(Sturniolo et al., 2016)

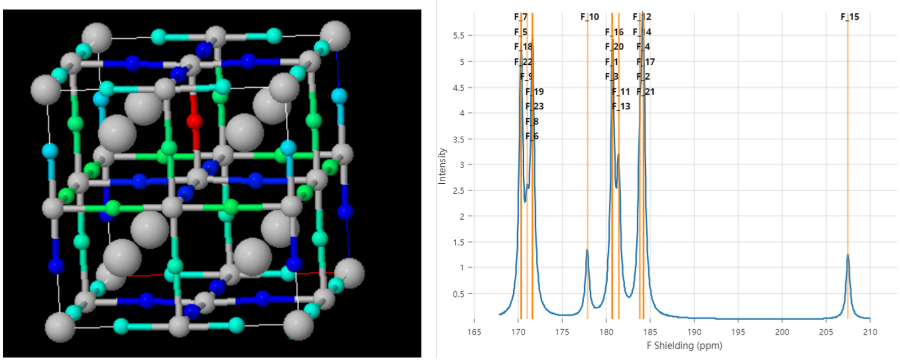

Figure 30: Visualization of the calculated isotropic chemical shielding data for the 2X2X2 supercell with F vacancy located at position 3. Left: the σ_{iso} for each individual F atom displayed in a color scale, with red being the one with the highest value and dark blue being the one with the lowest. Right: the σ_{iso} data for all F atoms showed in the spectrum form. Visualized using MagresView(Sturniolo et al., 2016)

A.2.3 2X2X4 supercell

Table 8: The ground state energy of the 2X2X4 supercell with the two F vacancies at different positions.

First F vacancy position	Second F vacancy position	Ground state energy (eV)
1	A	-119964.92
	B	-119965.26
	C	-119965.08
	D	-119963.72
2	A	-119964.30
	B	-119965.08
	C	-119965.26
	D	-119965.08

A.3 NEB calculations

The animations for the vacancy diffusion pathways in the 2X2X2 supercell that are used in the NEB calculations are linked below which are derived using Jmol(Jmol development team, 2023).
1-1: https://clipchamp.com/watch/EBECy7qvM6O
1-2: https://clipchamp.com/watch/hfGQ3BUn2XY
2-3: https://clipchamp.com/watch/W1zIy2lcjMH
1-3: https://clipchamp.com/watch/QmSFIwehu6m

Prior to obtaining the data shown in the results and discussion section. Two extra sets of NEB calculations are performed as can be seen from Fig 31 and Fig 32. The first set of NEB calculations directly used the cell structure generated after moving the atoms to the desired positions. From the results in Fig 31, it is pretty clear there are some other structures having even lower energy than the initial or final structure. Therefore, for the second set of NEB calculations, all the initial or final structures used first underwent a geometry optimization, and then the resulting structure is used for the NEB calculations.

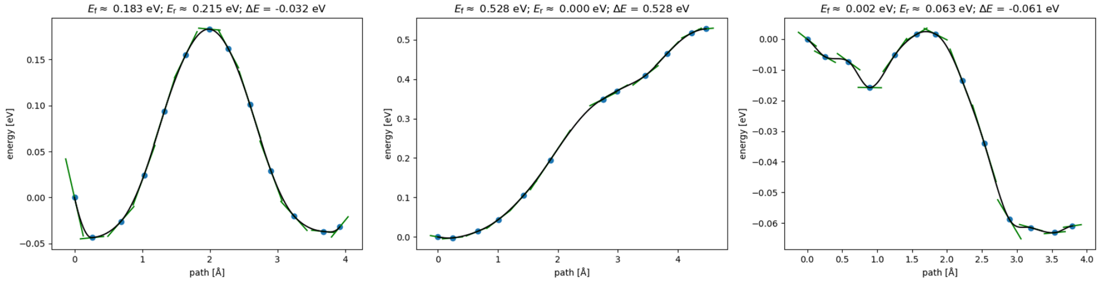

Figure 31: The first set of NEB calculations performed, from left to right, 1-1, 1-2, 2-3.

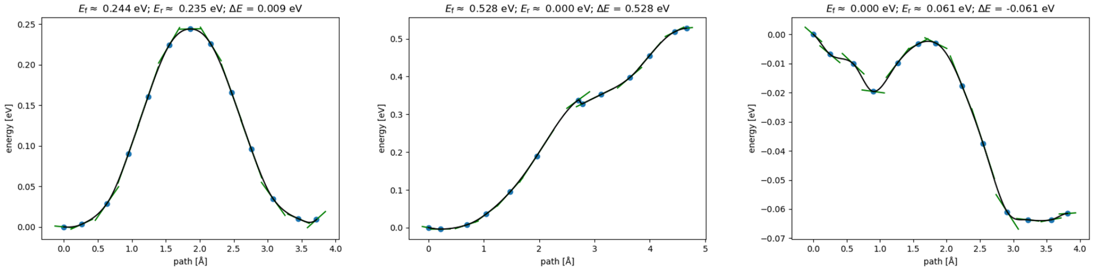

Figure 32: The second set of NEB calculations performed, from left to right, 1-1, 1-2, 2-3.

From what can be seen in Fig 32, the results are getting slightly better, but some not expected trends are still there. This could be potentially attributed to the fact that these calculations use a fixed lattice parameter when searching for the saddle points, while the initial and final structures inputted here do not have the same lattice parameters. Since these calculations are performed using Castep, no methods were found here to change the lattice parameter on the fly when running the NEB calculations. Therefore, to make the initial and final structures both the ones with the lowest energy already, the average lattice parameters for the two relaxed structures were used to optimize the initial and final cells again. Then the relaxed cells obtained after these optimizations are used to conduct the NEB calculations previously mentioned in the results and discussion section.

A.4 Example .cell file

```
%BLOCK lattice_cart
   ANG
       4.90369459156410       0.282580239096526E-08   0.805569469815663E-08
      0.282580239105604E-08    4.90369458763860      -0.305813364406164E-08
      0.805569469772686E-08  -0.305813364394641E-08    4.90369459371945
%ENDBLOCK lattice_cart

%BLOCK positions_frac
   F    -0.000000000019983       0.499999999826909      -0.000000000403043
   F     0.000000000024289      -0.000000000202091       0.499999999590797
   F     0.500000000042100      -0.000000000165747      -0.000000000400413
   Cs    0.499999999678063       0.500000000553381       0.500000001212714
   Pb    0.000000000275531      -0.000000000012451      -0.000000000000055
%ENDBLOCK positions_frac

FIX_COM : true

%BLOCK species_pot
   F         2|1.2|14|16|18|20:21(qc=7)
   Cs        2|2.2|4|4|5|50U:60:51(qc=5)
   Pb        3|2.2|7|8|9|50U:60:51U:61:52
%ENDBLOCK species_pot

SYMMETRY_TOL :     0.001000

%BLOCK symmetry_ops
# Symm. op. 1       E
          1.000000000000000       0.000000000000000       0.000000000000000
          0.000000000000000       1.000000000000000       0.000000000000000
          0.000000000000000       0.000000000000000       1.000000000000000
          0.000000000000000       0.000000000000000       0.000000000000000
%ENDBLOCK symmetry_ops

kpoint_mp_grid :    9   9   9
```

A.5 Example .param file

```
task                    magres
magres_task             nmr
xc_functional           PBE
cut_off_energy          750
elec_energy_tol         1e-8
finite_basis_corr       Auto
calculate_stress        True
write_checkpoint        None
data_distribution       Gvector
MAX_SCF_CYCLES          60
fix_occupancy           true
opt_strategy            speed
num_dump_cycles         0
write_formatted_density TRUE
calculate_densdiff      TRUE
```

A.6 Abbreviations

Abbreviation	**Full name**
DFT	Density functional theory
NMR	Nuclear magnetic resonance
LDA	Local density approximation
NEB	Nudged elastic band
GGA	Generalized gradient approximation
PW91	Perdew–Wang functional developed in 1991
PBE	Perdew–Burke–Ernzerhof functional
PBEsol	PBE functional revised for solids
BZ	Brillouin zone
IBZ	Irreducible Brillouin zone
σ_{iso}	Isotropic chemical shielding
E_{cut}	Energy cutoffs
USPPs	Ultrasoft pseudopotentials
PAW	Projector augmented wave
CASTEP	Cambridge Serial Total Energy Package
GIAO	Gauge-including atomic orbitals
LAPW	Linear Augmented Plane Wave
GIPAW	Gauge Including Projector Augmented Waves
PK10	$CsPb_{1-x}K_xF_{3-x}$ with x=0.1
MD	Molecular dynamics
MAS-NMR	Magic angle spinning nuclear magnetic resonance
EFG	Electric field gradient
VESTA	Visualization for Electronic and Structural Analysis